



Subduction metasomatism and collision-related metamorphic dehydration controls on the fertility of porphyry copper ore-forming high Sr/Y magma in Tibet

Song Wu ^a, Youye Zheng ^{a,b}, Xiang Sun ^{a,*}

^a State Key Laboratory of Geological Processes and Mineral Resources, and School of Earth Science and Resources, China University of Geosciences, Beijing 100083, China

^b State Key Laboratory of Geological Processes and Mineral Resources, and Faculty of Earth Resources, China University of Geosciences, Wuhan 430074, China



ARTICLE INFO

Article history:

Received 19 June 2015

Received in revised form 19 October 2015

Accepted 22 October 2015

Available online 24 October 2015

Keywords:

Oxygen fugacity

Water content

Post-collision porphyry deposit

Dabu

Tibet

ABSTRACT

Processes generating fertile magma and associated porphyry Cu deposits in post-collision tectonic settings remain uncertain. Dabu, located in the Gangdese porphyry Cu belt of southern Tibet, is a typical porphyry Cu-Mo deposit that formed in a post-collision setting. The deposit records two stages of magmatism: an Eocene (46 ± 1 Ma) barren monzogranite (EG); and a fertile Miocene (15 ± 1 Ma) monzogranite porphyry (MMP). These intrusions have similar Sr-Nd ($^{87}\text{Sr}/^{86}\text{Sr}_{(i)} = 0.70514$ to 0.70573 , $\epsilon\text{Nd(t)} = -2.78$ to $+0.77$) and zircon Hf ($\epsilon\text{Hf(t)} = +3.46$ to $+8.85$) isotopic compositions that fall within the range of the Palaeocene-Eocene Gangdese Batholith and the coeval Linzizong volcanics and plot on a mixing line between Tethyan basalts and Indian Ocean pelagic sediments. These features, coupled with the variable Sr/Nd, Sr/Th, Ba/Th, and Rb/Y ratios of the intrusions, are indicative of a common source involving basaltic lower crustal melts underplated during the Palaeocene and Eocene. The basaltic material was sourced from a mantle wedge that was metasomatized by Neo-Tethyan slab-derived fluids and oceanic sediments. The MMP, however, formed under a higher magmatic oxygen fugacity than did the EG, as indicated by their higher zircon $\text{Ce}^{4+}/\text{Ce}^{3+}$ ratios (87–1112) and higher $f\text{O}_2$ values ($\Delta\text{FMQ} = 5$), determined using ilmenite-magnetite mineral pairs. The decompression and discharge of SO_2 during the Linzizong volcanic event and the fractionation of magnetite could account for the low oxygen fugacity ($\text{Ce}^{4+}/\text{Ce}^{3+} = 58$ –164; $\Delta\text{FMQ} = -0.3$) of the EG as well the limited development of porphyry deposits associated with the Gangdese Batholith.

The MMP and Miocene mineralization-related intrusions within other Gangdese porphyry Cu deposits have high Sr/Y and V/Sc ratios and a negative correlation between Dy/Yb and SiO_2 , all of which are indicative of the crystallization of hornblende from a hydrous mafic melt. The EG and Gangdese Batholith, however, have low Sr/Y and V/Sc ratios and decreasing Sr concentrations over a wide range of SiO_2 contents, indicating that these intrusions formed from dry melts that had undergone significant plagioclase fractionation. Late-crystallized hornblende is generally present as small crystals within early formed feldspar phenocrysts in the EG, which is in good agreement with a rapid increase followed by a decrease in Y and Dy concentrations at ~ 60 wt.% SiO_2 . In addition, apatite in MMP has F (2.66–3.72%) and Cl (0.06–0.53%) volatile contents that are higher than those of apatite from EG (0.85–1.50% F and 0.02–0.03% Cl). These geochemical and mineralogical characteristics suggest that EG formed from a relatively dry magma with $<4.0\%$ H_2O , whereas MMP formed from a more hydrous magma with $>5.5\%$ H_2O . It is here proposed that long-lived subduction caused the high oxygen fugacity conditions of the arc magma by adding oxidized components to the sub-arc mantle in addition to F, Cl, S, and Cu. Long-term metamorphic dehydration resulted from the India-Asia collision, and subsequent crust thickening and shortening was responsible for the high water contents by continuously replenishing the basaltic melts at the base of the lower crust. Both subduction-related metasomatism and late-collision-related metamorphic dehydration controlled the genesis of fertile magma that formed the post-collision porphyry Cu-Mo deposits of southern Tibet.

© 2015 Elsevier B.V. All rights reserved.

1. Introduction

Porphyry Cu deposits are commonly found in volcanic-arc tectonic settings above subduction zones and are generally associated with intermediate to felsic calc-alkaline magma (Richards, 2003, 2009; Seedorff et al., 2005; Sillitoe, 2010; Hou et al., 2011; Deng et al., 2014a,b). Recent

* Corresponding author.

E-mail address: sunxiang8003@sina.com (X. Sun).

research, however, has identified numerous porphyry-type deposits that formed in non-arc or post-collision settings, including porphyry deposits in the Alpine–Himalayan Tethyan Orogen such as the Kerman porphyry belt in Iran, and the Gangdese, Yulong and Ailaoshan porphyry belts of Tibet and Yunnan (Hou et al., 2009; Shafiei et al., 2009; Richards et al., 2012; Lu et al., 2013, 2015; Mao et al., 2014; Richards, 2014; Zheng et al., 2015). A variety of models have been proposed to explain the source of the magma that formed these post-collision porphyry Cu deposits. Hou et al. (2011) suggest that the adakite-like magma is derived from the partial melting of a thickened juvenile mafic lower crust or a delaminated thickened lower crust and that the breakdown of amphibole within these eclogite and garnet amphibolite sources contributed to the generation of the highly oxidized and hydrous fertile magma that formed non-arc porphyry Cu deposits. Richards (2009, 2011b) suggests that the fertile magma that formed post-subduction porphyry deposits is probably the product of the remelting of previously subduction-modified mantle lithosphere or hydrous lower-crustal cumulates residual from the first stages of arc magmatism, which stresses the inheritance of previously subduction-associated arc magma features with abundant F, Cl, S and Cu, and high oxidation states (Shafiei et al., 2009; Li et al., 2011; Wu et al., 2014).

Lee et al. (2012) propose that remelting of Cu-rich pyroxenite cumulates triggered by magnetite crystallization and the onset of sulfide saturation in the deep roots of arcs are important steps in the generation of porphyry Cu deposits. The authors also emphasize that the magmatism-related thickness and maturity of continental arcs controls on the concentration of Cu in the resulting magma, rather than sourcing any Cu from the mantle or subducting slab (Chiaradia, 2013; Lee, 2013). Lu et al. (2015) propose that the ore-forming high Sr/Y porphyries in southern Tibet are derived from high-pressure differentiation of hydrous mafic partial melts of the mantle, rather than from the melting of a thickened mafic lower crust.

The high oxygen fugacity conditions during the formation of primary melts and the high water content of these melts are both critical for the generation of fertile magma and associated porphyry deposits (Sillitoe, 2010; Richards, 2011a,b; Sun et al., 2013a, 2015; Loucks, 2014). The reason for this is that water, as the most abundant volatile component, can lower the solidus of silicate assemblages, leading to the formation of a magmatic–hydrothermal ore-forming system. Such a system is dominated by hydrous melts and a water-rich volatile phase at shallow crustal levels with the decrease in temperature and pressure (Wolf and Wyllie, 1994; Eichelberger, 1995; Burnham, 1997; Richards, 2011b; Liu et al., 2012). In addition to water, chloride and sulfur are also critical components of economic porphyry Cu deposits, because chloride controls the partitioning of Cu and other base metals. Furthermore, sufficient chloride can transport large quantities of metals as chloride complexes in a hydrothermal fluid, whereas sufficient initial sulfur in magma can mobilize metals such as Cu and Mo from the asthenospheric mantle wedge above subduction zones and yield a sulfur-rich aqueous fluid (Cline and Bodnar, 1991; Cline, 1995; Pokrovski et al., 2008; Richards, 2015). A relatively high oxidation state of magma ensures that the bulk of the sulfur dissolved in the melt is present as sulfate, resulting in the retention of sulfide-compatible (i.e. chalcophile) elements in the evolving magma until they are partitioned into exsolving hydrothermal fluids (Carroll and Rutherford, 1985; Richards, 2003).

The Gangdese metallogenetic belt in Tibet contains porphyry Cu–Mo deposits that formed in a post-collisional setting, such as Qulong, Zhunuo, and Dabu (Zheng et al., 2004, 2007b, 2014a; Yang, 2008; Wu et al., 2014). The belt was subjected to a long-lived northward subduction of the Neo-Tethyan oceanic slab and the subsequent collision of the Indian and Asian plates (Zhu et al., 2013). Subduction-associated arc magma represented by the Palaeocene–Eocene Gangdese Batholith, however, has little potential of forming economic porphyry Cu deposits, especially when compared with Miocene intrusions in the area (Wen, 2007; Ji et al., 2009). Wang et al. (2014b,c) studied the temporal and geochemical evolution of igneous rocks along the eastern part of the

Gangdese magmatic belt in southern Tibet. They conclude that increasing magmatic water volume and oxygen fugacity from Palaeocene–Eocene to the Oligocene–Miocene magmatism is essential in the formation of post-subduction porphyry Cu deposits. Yang et al. (2015), however, suggest a mixing model involving ultra-potassic melts and melts derived from the juvenile lower crust to explain the high K₂O concentrations of adakite-like rocks in the Qulong porphyry Cu deposit. The authors emphasize that the water necessary for the formation of the porphyry Cu systems in continental collision zones is generally added by ultra-potassic magma instead of dehydrating slabs. These possibilities show that understanding the key factors and processes that control the fertility of Miocene mineralization-related intrusions in southern Tibet and whether the magma is linked to earlier subduction-related processes can provide important constraints on the genesis of post-collision porphyry deposits and guide mineral exploration in the area.

This manuscript presents a detailed petrographic, mineralogical, and geochemical comparison of a barren Eocene monzogranite (EG) with a fertile Miocene monzogranite porphyry (MMP) associated with the Dabu porphyry Cu–Mo deposit in southern Tibet. The oxidation state of the magma associated with the intrusions and the water contents of their initial melts are discussed here. This is followed by the comparison between the data collected in this study and published data for the Miocene ultra-potassic rocks in southern Tibet, the Gangdese Batholith, and the coeval Linzizong volcanics to further constrain the relationship and differences among these igneous rocks (Miller et al., 1999; Gao et al., 2007; Mo et al., 2007, 2008; Wen, 2007; Zhao et al., 2009; Ji et al., 2012; Lee et al., 2012; Liu et al., 2014; Wang et al., 2014a). These data are finally used to develop a new petrogenetic model that can account for the formation of both barren and fertile intrusive rocks associated with the Gangdese porphyry Cu deposits (GPCD).

2. Regional geology

The Tibetan Plateau is part of the Alpine–Himalayan orogenic belt and is divided into the Songpan–Ganzi, Qiangtang, Lhasa, and Himalaya terranes (Fig. 1a; Yin and Harrison, 2000). The Lhasa Terrane, also called the Gangdese orogenic belt, is a ~2500 km long tectono-magmatic belt (or domain) that is ~150–300 km wide and bound by the Bangong–Nujiang and Indus–Yarlung Zangbo sutures (Fig. 1b; Pan et al., 2006). The terrane is divided into northern, central, and southern domains that are separated by the Shiquanhe–Nam Tso Mélange Zone and the Luobadui–Milashan Fault (Fig. 1b; Zhu et al., 2011a). The central Lhasa Domain contains Precambrian rocks and either represents a microcontinent derived from the Australian Gondwana or has rifted off the Indian Gondwana (Yin and Harrison, 2000; Zhu et al., 2011b). In contrast, the southern and northern domains are characterized by juvenile crust with a locally preserved Precambrian crystalline substrate and were more recently accreted during their movement across the Tethyan Ocean (Ji et al., 2009; Zhu et al., 2011a; Hou et al., 2015a).

The Lhasa Terrane consists of Precambrian crystalline rocks unconformably overlain by Paleozoic to Mesozoic marine sedimentary units and arc-type volcanics, abundant Mesozoic and Cenozoic intrusions, and three medium- to high-grade metamorphic belts (Yin and Harrison, 2000; Pan et al., 2006; Zhu et al., 2013; Zhang et al., 2014b). Recently, authors have suggested that the eastern part of the terrane underwent amphibolite and granulite facies metamorphism during the Mesozoic and Cenozoic (e.g. Dong et al., 2010; Zhang et al., 2014b). The Gangdese Batholith and Linzizong volcanics formed as an Andean-style magmatic-arc along the southern flank of the terrane (Fig. 1b). These units are attributed to the northward subduction of Tethyan oceanic lithosphere from the Jurassic to the Palaeogene (Mo et al., 2008; Wen et al., 2008; Ji et al., 2009; Lee et al., 2012).

Post-collisional ultra-potassic rocks are located in the western part of the Lhasa Terrane, with ages ranging from 24 to 8 Ma, and commonly crop out along northward trending normal faults (Miller et al., 1999; Gao et al., 2007; Zhao et al., 2009; Liu et al., 2013; Wang et al., 2014a).

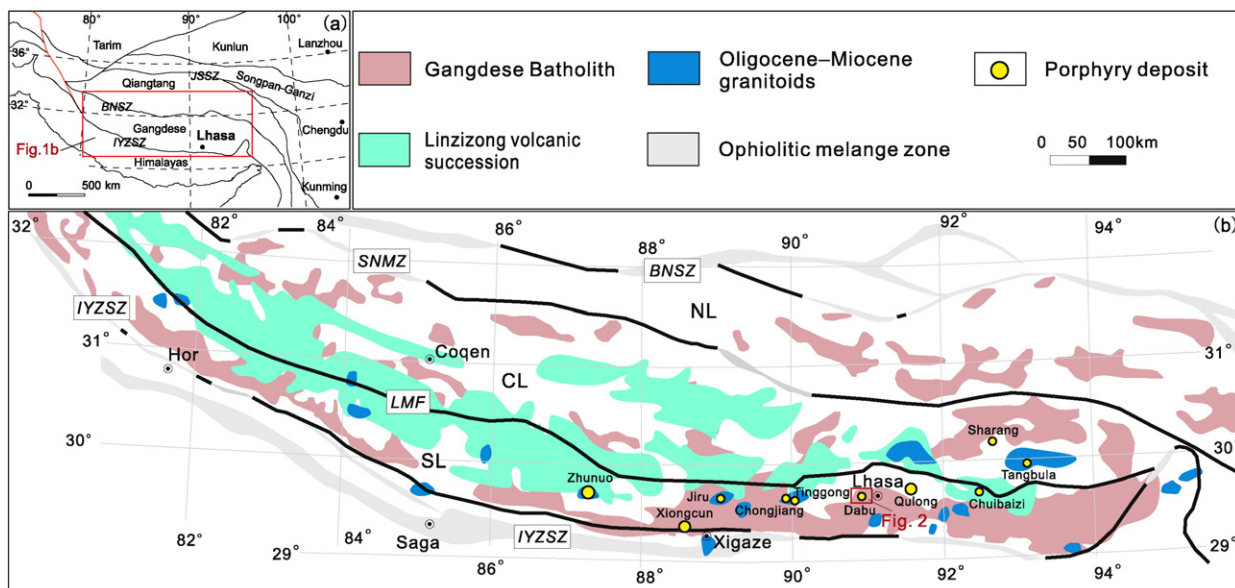


Fig. 1. (a) Tectonic framework of the Tibetan Plateau (Yin and Harrison, 2000); (b) simplified geological map of the Lhasa Terrane showing the distribution of the main porphyry deposits and the locality of the study area (modified after Zhu et al., 2011a; Wu et al., 2014; Mo et al., 2008). Abbreviations: JSSZ = Jinsha suture zone, BNSZ = Bangong–Nujiang suture zone, SNMZ = Shiquan River–Nam Tso Mélange Zone, LMF = Luobadui–Milashan Fault, IYSZ = Indus–Yarlung Zangbo Suture Zone, SL = southern Lhasa Domain, CL = central Lhasa Domain, NL = northern Lhasa Domain.

Oligocene–Miocene granitic rocks with high Sr/Y values are present as dykes and small intrusions within the southern Lhasa Domain and define an eastward trending magmatic belt along the Indus–Yarlung Zangbo Suture (Fig. 1b; Chung et al., 2009; Gao et al., 2010; Zheng et al., 2012; Zhang et al., 2014a).

Three episodes of porphyry-type mineralization, which formed in subduction, syn-collisional, and post-collisional tectonic settings between the Middle Jurassic and the Miocene, have been identified in southern Tibet (Hou et al., 2009, 2015b; Lang et al., 2014; Zhao et al., 2014; Zheng et al., 2014b). The post-collision porphyry Cu deposits are generally associated with Miocene intrusions with high Sr/Y values and define the giant eastward trending Gangdese porphyry Cu belt. The belt included the Zhunuo, Jiru, Chongjiang, Tinggong, Dabu, Lakang'e, Qulong, Demingding, Chuibaizi, and Tangbula deposits (Fig. 1b). These deposits have molybdenite Re–Os ages between ca. 21 and 13 Ma and are associated with mineralized ca. 20 and 13 Ma porphyritic intrusions (Zheng et al., 2015). Several porphyry–skarn Cu–W–Mo deposits are located within the SE margin of the Gangdese porphyry Cu belt, including the Mingze–Chengba and Nuri deposits, and are related to Oligocene granodiorite or monzonite intrusions (Chen et al., 2012; Sun et al., 2013c). The rocks in the Palaeocene–Eocene arc are predominantly barren, with only the Sharang porphyry Mo and Jiru porphyry Cu deposits present (Zhang et al., 2008; Zhao et al., 2014; Zheng et al., 2014b). The Xiongcuo deposit is a unique porphyry Cu–Au deposit that formed in response to northward subduction of Tethyan oceanic crust during the Jurassic (Lang et al., 2014). Overall, it is evident that subduction-related porphyry deposits are rare in southern Tibet, especially when compared to the size and number of collision-related porphyry deposits.

3. Deposit geology

The Dabu porphyry Cu–Mo deposit is located ~40 km west of Lhasa and is a typical example of a porphyry deposit that formed in a post-collisional setting. The deposit has a reserve of approximately 0.5 Mt Cu at an average grade of ~0.31 wt.% (Zheng et al., 2015). The deposit's age is ca. 15 ± 1 Ma, as constrained from U–Pb SHRIMP zircon dating of the

ore-forming monzogranite porphyry (Wu et al., 2014). This date is also consistent with the molybdenite Re–Os isochron age of ca. 15 ± 1 Ma for the deposit (Qu et al., 2007).

The rocks in the Dabu mine area include an Eocene medium- to coarse-grained monzogranite and Miocene medium- to fine-grained monzogranite porphyry and granodiorite. Eocene rocks are widespread throughout the area, which are cross-cut by small stocks or dykes of the MMP and granodiorite (Fig. 2). Ovoidal and ellipsoidal mafic microgranular enclaves are common in the Miocene monzogranite porphyry (Fig. 3b).

The Eocene rocks are light red in color and are not mineralized and not altered (Fig. 3a). They contain K-feldspar (35%), plagioclase (20%), quartz (35%), hornblende (5%), and biotite (5%). The K-feldspar ranges from 10 to 30 mm in size, forming euhedral megacrysts, whereas the plagioclase, quartz, hornblende, and biotite forming the matrix are subhedral to anhedral and relatively small (1–3 mm; Fig. 3c). The hornblende is usually present as small crystals within K-feldspar phenocrysts (Fig. 3e), indicating that it crystallized after the feldspars in more evolved melts. The porphyritic Miocene intrusions contain quartz (10%), plagioclase (30%), K-feldspar (15%), and biotite (4%) phenocrysts that range in size from 1 to 4 mm, as well as minor (~5%) amounts of magnetite, ilmenite, apatite, rutile, and sphene (Fig. 3d). The groundmass is microcrystalline or consists of aphanitic felsic minerals (Fig. 3f). These rocks are free of hornblende, indicating that they may have solidified from more primitive melts before the formation of the feldspar in the monzogranite porphyry.

The ore minerals at Dabu are hosted by the monzogranite porphyry and consist of veined or disseminated chalcopyrite, pyrite, lamellar molybdenite, and minor amounts of ragged magnetite (Fig. 4a, b, c). The deposit is dominated by potassic, phyllitic, and propylitic alteration. The potassic alteration is characterized by thin sheets of secondary biotite (Fig. 4d), disseminated secondary fine-grained K-feldspar crystals, quartz-K-feldspar veins surrounded by a micro-grain K-feldspar alteration halo (Fig. 4f), and is widely developed from the ground surface to deep parts of the deposit. The phyllitic alteration is weakly developed from the ground surface to a depth of ~200 m and is dominated by sericite locally replacing plagioclase (Fig. 4e). Propylitic alteration is only present within 100 m of the ground surface, and the deposit does not have a supergene enrichment zone or a leached cap.

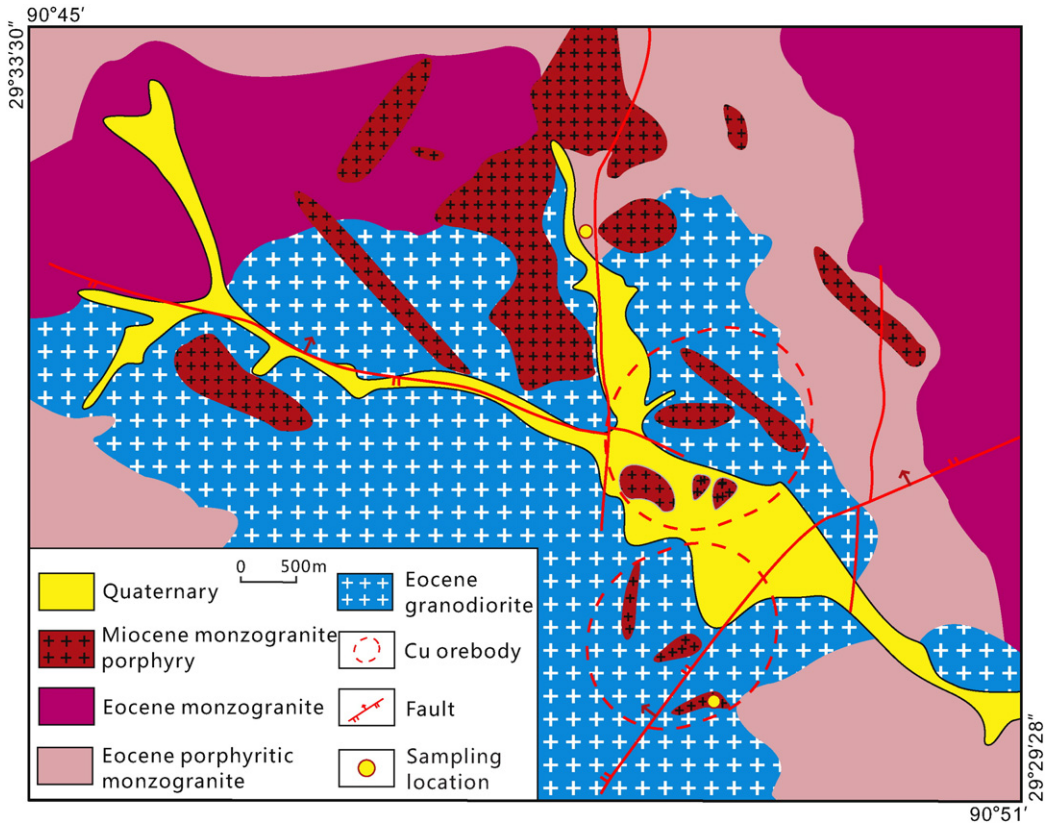


Fig. 2. Geological map of the Dabu porphyry Cu–Mo deposit.

4. Analytical methods

4.1. Zircon U–Pb dating

Zircons from Samples DB-18 and DB-75 were separated by conventional techniques involving rock crushing, sieving, drying, and electro-magnetic and heavy liquid separation at the Institute of Regional Geology and Mineral Resource Survey in the Hebei Province of China. Single zircon crystals from each sample were handpicked under a binocular microscope on the basis of size, clarity, color, and morphology. The crystals were then mounted in epoxy resin, polished to expose their crystal centers, and coated with gold. Transmitted and reflected light photomicrographs and cathodoluminescence (CL) images were taken to reveal any internal zoning and inheritance prior to analyses. CL images were obtained using a JEOL JXA-8100 microprobe at the Electron Microprobe Group of the Institute of Geology and Geophysics, Chinese Academy of Geological Sciences. Zircon U–Th–Pb isotope analyses were performed using a sensitive high-resolution ion microprobe (SHRIMP) from the SHRIMP II Consortium at Curtin University of Technology in Perth, Western Australia, based on the operating procedures and conditions described by Compston et al. (1984), Williams (1998), Lu et al. (2012) and Liu et al. (2015a). The ratios and absolute abundances of U, Th, and Pb isotopes were determined relative to the BR266 zircon standard ($^{206}\text{Pb}/^{238}\text{U}$ age = 559.0 ± 0.3 Ma; Stern, 2001). The TEMORA standard with an age of 417 Ma and a $^{206}\text{Pb}/^{238}\text{U}$ ratio of 0.0668 (Black et al., 2003) was used to monitor performance. Analyses of the BR266 standard were interspersed with zircon of unknown age during each measurement session. During the analytical period, several measurements of the BR266 zircon standard gave weighted mean $^{206}\text{Pb}/^{238}\text{U}$ ages of 546.5 ± 9.7 Ma (MSWD = 0.99, n = 3). A spot size between 25 and 30 μm in diameter was used during the analyses, with a mass-filtered O_2^- primary beam of ~ 2 nA. Measured compositions were corrected for common Pb using the ^{204}Pb method, and the programs SQUID II and ISOPLOT were used for data processing

(Ludwig, 2003, 2009). The uncertainties in individual analysis are reported at the 1σ level, and the mean ages of pooled $^{206}\text{Pb}/^{238}\text{U}$ results are quoted at the 95% confidence level.

4.2. In-situ zircon Hf isotope analyses

In-situ Hf isotope measurements were subsequently completed on the same spots or the same age domains for the age determinations of zircons with concordant ages, as guided by the CL images. Zircons were analyzed using a Neptune Plus multiple collector inductively coupled plasma mass spectrometer (MC-ICP-MS) coupled to a Geolas 2005 excimer ArF laser ablation system with a beam diameter of 44 μm at the state Key Laboratory of Geological Processes and Mineral Resources, China University of Geosciences in Wuhan. The GJ-1 and 91,500 zircon standards were analyzed to evaluate the accuracy of the laser-ablation results. During the session, GJ-1 yielded mean $^{176}\text{Hf}/^{177}\text{Hf}$ values of 0.282036 ± 10 (2σ , n = 8; the recommended value is 0.282015 ± 19 in Elhlou et al., 2006), and 91,500 gave a mean $^{176}\text{Hf}/^{177}\text{Hf}$ value of 0.282322 ± 28 (2σ , n = 26; the recommended value is 0.282330 ± 29 in Griffin et al., 2006). Detailed instrumental conditions and data acquisition are given in Hu et al. (2012). The $\epsilon\text{Hf}(t)$ values are parts of the 10^4 deviation of the initial Hf isotope ratios between the zircon sample and the chondritic reservoir, and T_{DM}^{C} denotes the zircon Hf isotope crustal model ages based on a depleted-mantle source and an assumption that the protolith of the zircon's host magma has the average continental crustal $^{176}\text{Lu}/^{177}\text{Hf}$ ratio of 0.015. The $\epsilon\text{Hf}(t)$ and T_{DM}^{C} values were calculated following the recommendation of Griffin et al. (2002) using the ^{176}Lu decay constant given by Blichert-Toft and Albarède (1997).

4.3. Zircon trace element analyses

Trace element analyses were performed on zircons using a laser-ablation, inductively coupled plasma mass spectrometer (LA-ICPMS) at the State Key Laboratory of Continental Dynamics, Northwest University

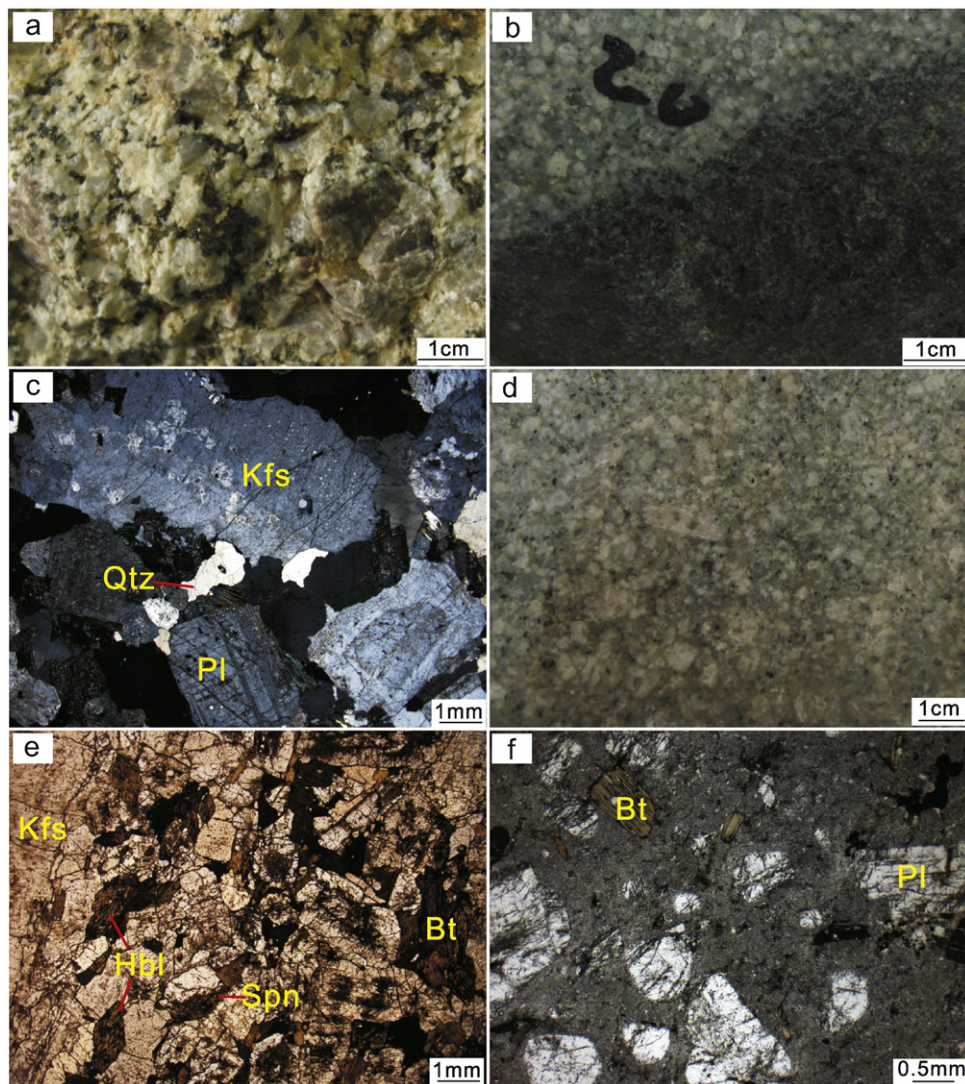


Fig. 3. Representative field and petrographic photographs of EG and MMP at the Dabu porphyry Cu-Mo deposit. (a, c) Porphyroid texture of the EG with euhedral K-feldspar megacrysts; (b) mafic enclaves hosted within MMP; (e) the small hornblende crystals within K-feldspar phenocrysts in EG; (d, f) typical porphyritic texture of MMP with quartz, plagioclase, and biotite. Abbreviations: Bt = biotite, Kfs = K-feldspar, Qtz = quartz, Pl = plagioclase, Hbl = hornblende, Spn = sphene.

in Xi'an, China. All of the measurements were carried out using time-resolved analysis operating in a fast, peak-jumping mode. Each spot analysis consisted of ~30 s of background acquisition (gas blank) followed by 60 s of data acquisition. The oxide production rate was tuned at <0.5% ThO/Th. NIST 610 glass was used as an external standard to calculate the trace-element concentrations of unknowns (Pearce et al., 1997). NIST 610 was run three times per sample, with one analysis at both the beginning and end and one analysis in the middle of each run. The ^{29}Si signatures were used to monitored mineral inclusions during analyses, and any analysis with an abnormal ^{29}Si signature was discarded. Data reduction was performed using the GLITTER 4.0 Macquarie University software. A detailed compilation of instrument and data acquisition parameters is given by Gao et al. (2002) and Yuan et al. (2004).

4.4. Sr-Nd isotope analyses

Whole-rock Sr-Nd isotope analyses were performed at the state Key Laboratory of Geological Processes and Mineral Resources, China University of Geosciences in Wuhan. The Sr isotope ratios were determined using a Finnigan Triton TIMS. During the analytical period, several measurements of the NBS987 Sr reference standard yielded $^{87}\text{Sr}/^{86}\text{Sr}$ values of 0.71025 ± 8 (2σ ; the recommended value is 0.71024), and the

Chinese GBW04411 standard yielded $^{87}\text{Sr}/^{86}\text{Sr}$ values of 0.75999 ± 4 (the recommended value is 0.75999 ± 20). Mass fractionation was corrected to $^{87}\text{Sr}/^{86}\text{Sr} = 0.1194$.

Nd isotope composition analyses were carried out on a Neptune multiple collector inductively coupled plasma mass spectrometer (MC-ICP-MS). The international BCR-2 Nd reference solution yielded $^{143}\text{Nd}/^{144}\text{Nd}$ values of 0.512643 ± 15 (2σ ; the recommended value is 0.512633), and the international JNd-1 standard yielded $^{143}\text{Nd}/^{144}\text{Nd}$ values of 0.512115 ± 8 (2σ ; the recommended value is 0.512115). The Nd isotope ratios were internally corrected for mass fractionation using a constant value of 0.7219 for $^{146}\text{Nd}/^{144}\text{Nd}$ by exponential law. The $^{147}\text{Sm}/^{144}\text{Nd}$ and $^{87}\text{Rb}/^{86}\text{Sr}$ ratios of the samples were calculated using Sm, Nd, Rb, and Sr concentrations determined on an ICP-MS (eg. Liang and Grégoire, 2000). The total analytical blanks were <50 pg for Nd and 0.2–0.5 ng for Sr. The detailed procedures for sample digestion, column chemistry, and instrumental analysis are described in Ling et al. (2009).

4.5. Major and trace element analyses

Whole-rock chemical analyses were determined at the Institute of Regional Geology and Mineral Resource Survey of the Hebei Province, China. The samples were ground to ~200 mesh in an agate mortar. The

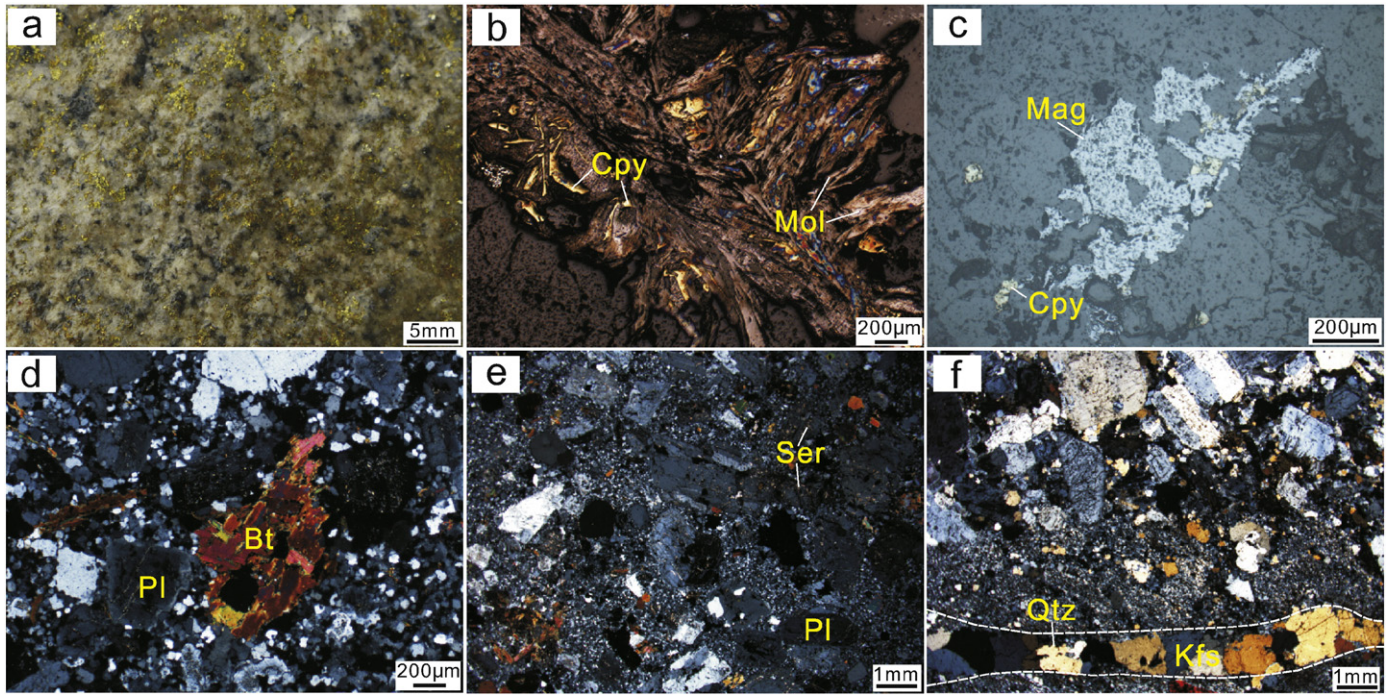


Fig. 4. Photographs showing characteristics of the alteration and mineralization at the Dabu deposit: (a) disseminated chalcopyrite and pyrite; (b) clusters of anhedral chalcopyrite and lamellar molybdenite; (c) interstitial texture of euhedral-ragged magnetite and anhedral-granular chalcopyrite; (d) thin secondary biotite with distinct cleavage and pleochroism; (e) weak phyllitic alteration dominated by sericite that is locally replaced plagioclase; (f) quartz-K-feldspar vein surrounded by a micro-grain K-feldspar alteration halo. Abbreviations: Cpy = chalcopyrite, Mol = molybdenite, Mag = magnetite, Ser = sericite.

major oxides were determined using X-ray fluorescence spectrometry (XRF) on fused glass disks, and the standard GB/T14506.28-1993 for Na_2O , MgO , Al_2O_3 , SiO_2 , P_2O_5 , K_2O , CaO , TiO_2 , MnO , Fe_2O_3 , and FeO . The standard GB/T14506.2-1993 was used for H_2O^+ , and the standard LY/T 1253-1999 was used for loss-on-ignition (LOI). Rare earth elements (REE) and trace elements including Cu, Pb, Th, U, Hf, Ta, Sc, Cs, V, Co, and Ni were determined using ICP-MS and the standard DZ/T 0223-2001. The elements Sr, Ba, Zn, Rb, Nb, Zr, and Ga were determined using XRF on pressed powder pellets and the standard JY/T016-1996. A blank solution was prepared, and the total procedural blank was <50 ng for all elements assayed. The analyses were crosschecked using different analytical methods and verified by reference to the international GBW standard. The estimated precision for most elements varied from 1 to 10%. Liang and Grégoire (2000) describe the analytical procedures, which are similar to those described by Wu et al. (2009) and Liu et al. (2015b).

4.6. Electron microprobe analyses

Mineral chemistry analyses of silicates and oxides were determined on polished thin sections using a JXA-8230 electron microprobe at the Institute of Mineral Resources, Chinese Academy of Geological Sciences. Analyses of Si, Al, Fe_{To} , Mg, Ti, Mn, Ca, Na, K, P, Cr, and Ni were completed for biotite, apatite, magnetite, and ilmenite using an accelerating voltage of 15 kV at a beam current of 20 nA and a spot diameter of 5 μm . Natural minerals and synthetic pure oxides were used as standards. Liu et al. (2015c, 2015d) describe the matrix corrections using the ZAF correction program, standards, and crystals during the analyses of some elements.

5. Results

5.1. Zircon U-Pb ages

Zircon U-Pb isotopic results for EG and MMP are presented in Table 1 and plotted on Fig. 5. Eleven spot analyses of zircons from EG contain 156–620 ppm U and 89–526 ppm Th with high Th/U ratios of 0.42 to 0.92, indicating that they are of magmatic origin (Hoskin and

Black, 2000). Their $^{206}\text{Pb}/^{238}\text{U}$ ages have a weighted mean of 46 ± 1 Ma (2σ , MSWD = 1.4; Fig. 5c), which is interpreted as the crystallization age of EG. Zircons from MMP contain 101–1493 ppm Th and 116–1183 ppm U with Th/U ratios of 0.68–1.78. Analyses of nine grains form a coherent age group with a weighted mean age of 15 ± 1 Ma (2σ , MSWD = 1.5; Fig. 5d). The remainder spot analysis of zircon with a dark core yielded an age of 46 Ma, which is consistent with the age of EG within error and interpreted as a date for inherited zircon in EG.

5.2. Major and trace elements

The major and trace element compositions of MMP and EG at the Dabu deposit are listed in Table 2. The MMP has a felsic composition with SiO_2 contents ranging from 65.5 to 70.3 wt.% and high alkali contents ($\text{Na}_2\text{O} + \text{K}_2\text{O}$) varying from 6.9 to 8.9 wt.%. The MMP plots in the monzogranite and granodiorite fields on the $\text{K}_2\text{O} + \text{Na}_2\text{O}$ versus SiO_2 diagram of Middlemost (1994) (Fig. 6a). The K_2O versus SiO_2 (wt.%) diagram in Fig. 6b shows that MMP can be classified as high-K calc-alkaline series that also have high Sr (494–952 ppm) and low Y (5.6–7.1 ppm) contents, resulting in moderately high Sr/Y ratios (83.6–164.5) (Fig. 6b, c). The MMP is strongly fractionated in REE, as shown in Fig. 7a with a La_N/Yb_N ratio of 19.7–33.2, does not have an Eu anomaly ($\text{Eu}/\text{Eu}^* = 0.87$ –1.08), and has highly fractionated middle REE (MREE) to heavy REE (HREE) with Sm_N/Yb_N (5.5–8.2) and Gd_N/Yb_N (2.7–4.1) ratios. MMP samples are also enriched in Pb, Hf, and K elements, but are depleted in Nb, Ta, Zr, Ti, and P on the primitive mantle-normalized plot (Fig. 7b). Such trace element characteristics are indicative of the involvement of garnet and amphibole as cumulates or residual phases in the parent magma (e.g. Martin et al., 2005; Moyen, 2009; Gao et al., 2009). The EG has an intermediate SiO_2 composition ranging from 62.4 to 66.0 wt.% with a high alkali content ($\text{Na}_2\text{O} + \text{K}_2\text{O}$) varying from 7.7 to 8.7 wt.%, plots in the high-K calc-alkaline and shoshonitic fields on Fig. 6b, and is marked by low Sr/Y and La/Yb ratios compared to the MMP (Fig. 6c, d). In addition, EG has moderately fractionated light REE (LREE) to HREE ($\text{La}_N/\text{Yb}_N = 17.8$ –23.2) with relatively flat middle to heavy patterns ($\text{Sm}_N/\text{Yb}_N = 3.89$ –4.75; $\text{Gd}_N/\text{Yb}_N = 2.18$ –2.84), LREE enrichment, and a

Table 1

Zircon SHRIMP U-Pb data for EG (DB-75) and MMP (DB-18) at the Dabu porphyry deposit.

| Spot | U (ppm) | Th (ppm) | Th/U | $^{206}\text{Pb}_c$ (%) | $^{206}\text{Pb}^a$ (ppm) | $^{207}\text{Pb}^{235}\text{U}$ ($\pm\%$) | $^{206}\text{Pb}^{238}\text{U}$ ($\pm\%$) | $^{206}\text{Pb}^{238}\text{U}$ (Ma; $\pm 1\sigma$) |
|----------------------|---------|----------|------|-------------------------|---------------------------|---|---|--|
| <i>DB-75 for EG</i> | | | | | | | | |
| 1.1 | 377 | 348 | 0.92 | 3.55 | 2.27 | 0.030(34) | 0.00700(2.4) | 45.0(1.1) |
| 2.1 | 325 | 275 | 0.85 | — | 2.06 | 0.054(9) | 0.00739(2.2) | 47.5(1.0) |
| 3.1 | 347 | 147 | 0.42 | — | 2.15 | 0.054(9) | 0.00722(1.7) | 46.4(0.8) |
| 4.1 | 1405 | 2028 | 1.44 | — | 9.25 | 0.051(5) | 0.00767(1.9) | 49.2(0.9) |
| 5.1 | 460 | 334 | 0.73 | — | 2.89 | 0.050(7) | 0.00731(1.6) | 47.0(0.8) |
| 6.1 | 434 | 299 | 0.69 | 0.33 | 2.68 | 0.048(9) | 0.00719(1.7) | 46.2(0.8) |
| 7.1 | 246 | 199 | 0.81 | 2.91 | 1.43 | 0.027(45) | 0.00678(2.3) | 43.5(1.0) |
| 8.1 | 212 | 122 | 0.58 | 1.39 | 1.30 | 0.033(29) | 0.00715(3.9) | 45.9(1.8) |
| 9.1 | 342 | 246 | 0.72 | 0.98 | 2.13 | 0.038(18) | 0.00724(1.8) | 46.5(0.8) |
| 10.1 | 156 | 89 | 0.57 | 0.97 | 0.97 | 0.035(27) | 0.00720(2.7) | 46.2(1.2) |
| 11.1 | 391 | 225 | 0.57 | 1.76 | 2.32 | 0.034(22) | 0.00690(2.4) | 44.3(1.0) |
| 12.1 | 620 | 526 | 0.85 | — | 3.83 | 0.057(8) | 0.00720(1.7) | 46.2(0.8) |
| <i>DB-18 for MMP</i> | | | | | | | | |
| 1.1 | 334 | 227 | 0.68 | 3.21 | 0.64 | 0.010(61) | 0.00223(3.4) | 14.4(0.4) |
| 2.1 | 273 | 486 | 1.78 | 0.00 | 0.55 | 0.014(17) | 0.00234(4.0) | 14.9(0.9) |
| 3.1 | 138 | 112 | 0.81 | 16.24 | 0.22 | 0.026(33) | 0.00188(10.7) | 14.4(0.8) |
| 4.1 | 104 | 77 | 0.73 | — | 0.25 | 0.062(31) | 0.00277(7.9) | 15.1(0.8) |
| 5.1 | 1183 | 1493 | 1.26 | — | 7.33 | 0.049(5) | 0.00722(1.9) | 46.4(1.0) |
| 6.1 | 114 | 89 | 0.78 | 27.03 | 0.16 | 0.048(40) | 0.00168(15.5) | 14.5(0.6) |
| 7.1 | 116 | 104 | 0.90 | 0.00 | 0.24 | 0.032(18) | 0.00242(5.5) | 14.7(1.0) |
| 8.1 | 172 | 134 | 0.78 | — | 0.36 | 0.024(33) | 0.00244(3.6) | 15.1(0.5) |
| 9.1 | 116 | 129 | 1.11 | 4.04 | 0.25 | 0.008(155) | 0.00253(4.6) | 16.5(0.5) |
| 10.1 | 162 | 78 | 0.48 | 2.94 | 0.36 | 0.010(99) | 0.00261(3.5) | 16.9(0.5) |
| 11.1 | 287 | 299 | 1.04 | 3.37 | 0.56 | 0.011(62) | 0.00228(3.0) | 14.9(0.4) |
| 12.1 | 106 | 112 | 1.06 | — | 0.23 | 0.023(19) | 0.00249(2.0) | 15.9(0.5) |
| 13.1 | 147 | 121 | 0.82 | 6.96 | 0.26 | 0.009(149) | 0.00208(5.6) | 14.6(0.4) |
| 14.1 | 151 | 126 | 0.83 | 3.36 | 0.29 | 0.009(103) | 0.00225(8.9) | 14.4(1.0) |
| 15.1 | 243 | 286 | 1.18 | 2.26 | 0.49 | 0.016(42) | 0.00233(4.8) | 15.3(0.9) |

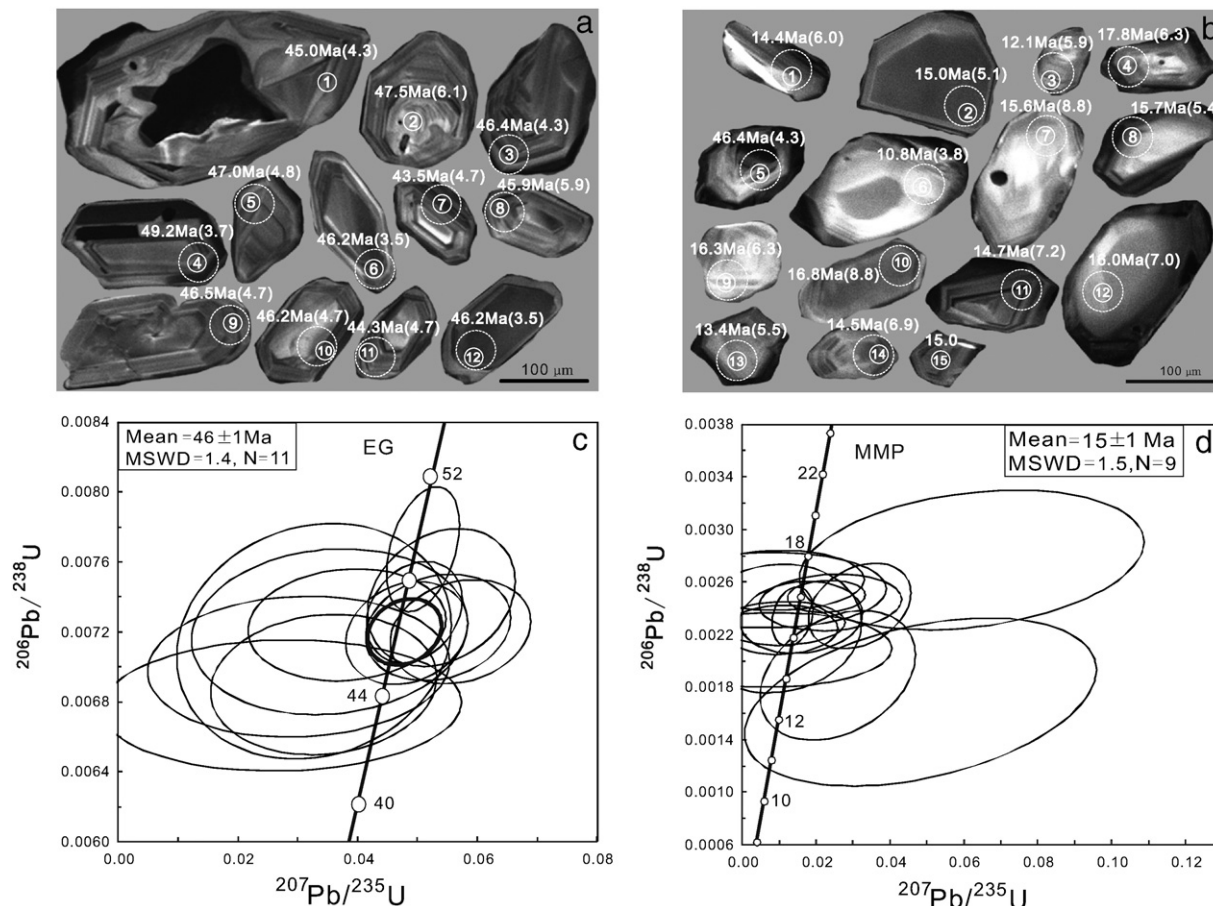
Note: $^{206}\text{Pb}_c$ denotes the proportion of common ^{206}Pb in total measured ^{206}Pb .^a Denotes radiogenic lead.**Fig. 5.** Cathodoluminescence images and concordia plots of zircons for EG (a, c) and MMP (b, d) at the Dabu deposit. Solid and dashed circles mark the area for U-Pb isotopic dating and Hf isotopic analysis of the zircons, respectively. The numbers in the solid circles denote the number of analysis spots. The SHRIMP U-Pb ages and $\epsilon\text{Hf}(t)$ values are given for each spot.

Table 2

Whole-rock major (wt.%) and trace element (ppm) data for EG and MMP at the Dabu porphyry deposit.

| Sample | DB11-35 | DB11-36 | DB11-76 | DB11 | DB13 | D-14 | DB15 | DB16 | DB17 | DB4-1 | DB4-2 | DB11-27 | DB11-49 | DB11-55 | DB11-60 | DB11-15 | DB11-72 | |
|--------------------------------|---------|---------|---------|--------|--------|--------|--------|--------|-------|--------|--------|---------|---------|---------|---------|---------|---------|--|
| | EG | | | | | | | | | MMP | | | | | | | | |
| SiO ₂ | 65.98 | 63.68 | 65.36 | 63.49 | 63.58 | 62.55 | 62.52 | 62.43 | 63.97 | 65.53 | 66.11 | 69.73 | 70.32 | 68.59 | 67.92 | 66.50 | 69.24 | |
| Al ₂ O ₃ | 15.50 | 16.10 | 16.60 | 16.39 | 16.30 | 16.70 | 16.34 | 16.70 | 15.85 | 16.39 | 16.55 | 15.31 | 15.23 | 15.65 | 16.11 | 16.52 | 16.05 | |
| TiO ₂ | 0.74 | 0.80 | 0.67 | 0.80 | 0.81 | 0.81 | 0.92 | 0.91 | 0.69 | 0.48 | 0.48 | 0.30 | 0.28 | 0.41 | 0.41 | 0.45 | 0.40 | |
| Fe ₂ O ₃ | 2.47 | 2.63 | 1.41 | 2.12 | 2.10 | 2.13 | 2.32 | 2.44 | 2.48 | 1.00 | 1.28 | 1.02 | 1.04 | 1.05 | 0.98 | 1.43 | 1.16 | |
| FeO | 1.68 | 2.16 | 1.51 | 2.18 | 2.23 | 2.37 | 2.49 | 2.35 | 1.99 | 2.06 | 1.89 | 1.10 | 0.79 | 1.63 | 1.65 | 1.51 | 0.36 | |
| CaO | 3.05 | 3.15 | 3.14 | 3.59 | 3.75 | 3.97 | 4.02 | 4.24 | 3.08 | 3.00 | 3.49 | 2.61 | 1.84 | 2.05 | 2.30 | 2.55 | 0.96 | |
| MgO | 1.63 | 1.83 | 1.44 | 1.67 | 1.65 | 1.80 | 1.90 | 1.81 | 1.54 | 1.67 | 1.66 | 1.02 | 0.94 | 1.22 | 1.20 | 1.47 | 1.15 | |
| K ₂ O | 3.44 | 3.95 | 4.48 | 4.20 | 3.84 | 3.62 | 3.54 | 3.09 | 5.03 | 2.31 | 2.23 | 3.13 | 3.80 | 3.21 | 3.05 | 2.84 | 3.77 | |
| Na ₂ O | 4.28 | 4.40 | 4.12 | 4.19 | 4.45 | 4.73 | 4.54 | 4.90 | 3.69 | 4.70 | 4.67 | 4.53 | 4.24 | 4.65 | 4.83 | 4.57 | 5.13 | |
| MnO | 0.028 | 0.031 | 0.066 | 0.079 | 0.078 | 0.082 | 0.088 | 0.085 | 0.075 | 0.034 | 0.047 | 0.031 | 0.020 | 0.021 | 0.023 | 0.020 | 0.019 | |
| P ₂ O ₅ | 0.296 | 0.320 | 0.262 | 0.332 | 0.339 | 0.353 | 0.369 | 0.356 | 0.290 | 0.194 | 0.195 | 0.139 | 0.110 | 0.158 | 0.158 | 0.177 | 0.167 | |
| LOI | 0.72 | 0.74 | 0.71 | 0.49 | 0.39 | 0.40 | 0.44 | 0.22 | 0.81 | 1.24 | 0.93 | 0.89 | 1.16 | 1.12 | 1.06 | 1.63 | 1.34 | |
| Total | 99.79 | 99.78 | 99.76 | 99.53 | 99.51 | 99.50 | 99.49 | 99.52 | 99.49 | 98.61 | 99.52 | 99.79 | 99.77 | 99.75 | 99.69 | 99.67 | 99.76 | |
| Mg# | 42.79 | 42.12 | 48.14 | 42.26 | 41.81 | 42.96 | 42.67 | 41.65 | 39.52 | 50.24 | 49.39 | 47.62 | 49.41 | 45.93 | 45.86 | 48.52 | 59.53 | |
| Be | 2.62 | 2.74 | 2.77 | 2.48 | 2.98 | 2.76 | 2.80 | 3.30 | 2.14 | 2.10 | 2.07 | 2.45 | 2.17 | 2.07 | 2.05 | 2.17 | | |
| Sc | 8.96 | 9.71 | 7.41 | 9.16 | 9.41 | 9.34 | 9.89 | 9.39 | 8.91 | 7.09 | 7.34 | 3.95 | 3.26 | 4.72 | 4.90 | 5.14 | 2.63 | |
| V | 77.7 | 85.1 | 64.9 | 97.8 | 105.6 | 97.8 | 111.3 | 109.7 | 104.1 | 80.5 | 85.6 | 38.7 | 34.4 | 61.7 | 62.3 | 58.1 | 56.2 | |
| Cr | 16.3 | 20.3 | 13.3 | 16.0 | 19.1 | 16.8 | 19.6 | 18.8 | 22.6 | 19.8 | 23.0 | 22.0 | 15.0 | 15.4 | 17.6 | 14.8 | 13.4 | |
| Co | 6.83 | 7.40 | 7.67 | 10.1 | 10.9 | 10.6 | 11.8 | 11.0 | 9.6 | 8.6 | 9.8 | 5.50 | 4.64 | 7.17 | 7.07 | 7.40 | 3.40 | |
| Ni | 5.96 | 5.85 | 4.95 | 6.4 | 7.3 | 6.5 | 7.5 | 7.3 | 6.2 | 16.8 | 16.5 | 8.88 | 7.14 | 7.07 | 7.71 | 11.21 | 6.60 | |
| Zn | 39.5 | 36.5 | 77.0 | 76.3 | 82.7 | 76.5 | 87.4 | 81.0 | 77.2 | 40.8 | 52.3 | 24.6 | 25.3 | 19.6 | 25.0 | 17.6 | 25.4 | |
| Ga | 21.6 | 21.6 | 21.9 | 20.9 | 22.3 | 20.9 | 22.1 | 22.2 | 19.9 | 19.7 | 20.1 | 17.1 | 17.6 | 20.1 | 21.8 | 19.8 | 18.5 | |
| Rb | 79.3 | 86.0 | 79.3 | 100.2 | 99.2 | 88.2 | 93.3 | 81.1 | 110.5 | 93.3 | 65.6 | 71.7 | 82.9 | 80.8 | 59.6 | 83.6 | 66.0 | |
| Sr | 622.9 | 638.4 | 706.7 | 750 | 753 | 768 | 753 | 769 | 736 | 914 | 952 | 646.5 | 616.5 | 716.9 | 764.7 | 630.8 | 494.3 | |
| Y | 20.13 | 22.63 | 21.59 | 18.74 | 19.09 | 17.77 | 22.27 | 20.11 | 15.15 | 5.56 | 6.74 | 6.94 | 5.76 | 6.73 | 6.37 | 7.11 | 5.91 | |
| Zr | 231.1 | 257.8 | 209.0 | 225.8 | 222.8 | 233.6 | 259.6 | 248.7 | 199.3 | 107.7 | 108.8 | 94.0 | 89.5 | 114.4 | 114.9 | 96.1 | 114.3 | |
| Nb | 24.22 | 23.10 | 22.15 | 22.00 | 23.42 | 20.89 | 25.55 | 25.36 | 17.88 | 2.70 | 5.42 | 5.75 | 3.21 | 3.58 | 4.07 | 3.57 | 2.43 | |
| Cs | 5.95 | 6.74 | 4.78 | 4.82 | 4.75 | 4.73 | 4.90 | 4.63 | 4.58 | 6.20 | 5.51 | 1.59 | 3.91 | 2.92 | 2.43 | 10.41 | 2.63 | |
| Ba | 866.7 | 946.8 | 1292 | 1270 | 1170 | 917 | 975 | 739 | 1558 | 698 | 795 | 833.4 | 853.4 | 900.9 | 1079 | 665.6 | 784.4 | |
| La | 69.74 | 65.94 | 61.77 | 51.66 | 56.65 | 54.11 | 65.44 | 59.35 | 43.95 | 19.26 | 22.32 | 21.45 | 21.92 | 28.98 | 26.73 | 23.85 | 22.80 | |
| Ce | 114.8 | 125.5 | 117.7 | 103.60 | 109.92 | 101.00 | 125.89 | 115.50 | 84.86 | 35.45 | 42.54 | 41.36 | 40.22 | 54.14 | 50.23 | 46.97 | 43.94 | |
| Pr | 15.19 | 16.93 | 15.92 | 12.01 | 12.49 | 11.47 | 14.61 | 13.13 | 9.72 | 4.25 | 5.15 | 6.04 | 5.62 | 7.62 | 7.09 | 6.87 | 6.38 | |
| Nd | 52.90 | 58.88 | 56.29 | 45.75 | 47.14 | 43.60 | 55.70 | 49.62 | 36.94 | 17.30 | 20.82 | 23.35 | 20.74 | 28.25 | 26.52 | 26.36 | 23.60 | |
| Sm | 8.29 | 9.34 | 8.86 | 7.35 | 7.42 | 6.95 | 8.80 | 7.94 | 5.96 | 2.92 | 3.50 | 4.11 | 3.43 | 4.43 | 4.11 | 4.33 | 3.66 | |
| Eu | 1.93 | 2.18 | 2.16 | 1.70 | 1.82 | 1.74 | 2.05 | 1.82 | 1.49 | 0.92 | 0.92 | 1.03 | 0.92 | 1.21 | 1.16 | 1.09 | 0.91 | |
| Gd | 6.25 | 6.99 | 6.55 | 5.81 | 6.01 | 5.57 | 7.09 | 6.42 | 4.79 | 2.10 | 2.54 | 2.59 | 2.36 | 3.09 | 2.87 | 2.80 | 2.48 | |
| Tb | 0.92 | 1.05 | 0.99 | 0.81 | 0.81 | 0.77 | 0.98 | 0.86 | 0.65 | 0.28 | 0.33 | 0.36 | 0.32 | 0.40 | 0.38 | 0.39 | 0.33 | |
| Dy | 4.31 | 4.79 | 4.63 | 3.60 | 3.67 | 3.73 | 4.10 | 3.96 | 2.85 | 1.11 | 1.36 | 1.59 | 1.33 | 1.62 | 1.56 | 1.60 | 1.35 | |
| Ho | 0.79 | 0.87 | 0.84 | 0.62 | 0.64 | 0.62 | 0.76 | 0.69 | 0.50 | 0.20 | 0.23 | 0.27 | 0.22 | 0.27 | 0.25 | 0.28 | 0.22 | |
| Er | 2.37 | 2.61 | 2.50 | 1.82 | 1.75 | 1.76 | 2.09 | 1.93 | 1.39 | 0.53 | 0.65 | 0.77 | 0.68 | 0.76 | 0.71 | 0.83 | 0.61 | |
| Tm | 0.37 | 0.40 | 0.38 | 0.27 | 0.28 | 0.26 | 0.33 | 0.29 | 0.21 | 0.07 | 0.09 | 0.11 | 0.09 | 0.10 | 0.09 | 0.12 | 0.08 | |
| Yb | 2.37 | 2.62 | 2.49 | 1.79 | 2.08 | 1.67 | 2.30 | 1.88 | 1.39 | 0.44 | 0.52 | 0.70 | 0.67 | 0.63 | 0.60 | 0.87 | 0.50 | |
| Lu | 0.31 | 0.35 | 0.34 | 0.22 | 0.23 | 0.22 | 0.36 | 0.25 | 0.19 | 0.06 | 0.08 | 0.11 | 0.11 | 0.09 | 0.10 | 0.11 | 0.08 | |
| Hf | 14.66 | 17.01 | 12.36 | 15.71 | 15.54 | 13.43 | 16.64 | 15.39 | 9.21 | 5.91 | 6.40 | 3.92 | 3.37 | 3.45 | 3.12 | 5.45 | 4.02 | |
| Ta | 1.86 | 1.81 | 1.86 | 1.65 | 1.69 | 1.51 | 1.86 | 1.84 | 1.27 | 0.17 | 0.38 | 0.46 | 0.27 | 0.31 | 0.25 | 0.17 | | |
| Pb | 13.6 | 15.8 | 21.0 | 24.3 | 24.2 | 19.3 | 20.8 | 20.2 | 24.2 | 19.0 | 18.1 | 17.6 | 45.9 | 24.3 | 30.4 | 17.1 | 20.6 | |
| Ti | 4437 | 4779 | 3999 | 4809 | 4827 | 4833 | 5528 | 5450 | 4161 | 2860 | 2878 | 1775 | 1679 | 2440 | 2446 | 2668 | 2398 | |
| Th | 17.50 | 15.47 | 19.80 | 16.2 | 13.7 | 10.7 | 15.1 | 12.9 | 10.9 | 9.0 | 7.8 | 16.47 | 12.76 | 11.59 | 10.57 | 11.54 | 7.00 | |
| U | 2.84 | 3.69 | 3.98 | 4.29 | 4.05 | 3.19 | 3.83 | 3.56 | 3.04 | 1.97 | 1.12 | 2.90 | 2.30 | 0.89 | 0.96 | 2.30 | 0.88 | |
| Eu/Eu* | 0.79 | 0.79 | 0.83 | 0.77 | 0.81 | 0.83 | 0.77 | 0.76 | 0.82 | 1.08 | 0.90 | 0.90 | 0.93 | 0.95 | 0.98 | 0.90 | 0.87 | |
| Nb/Ta | 13.01 | 12.79 | 11.93 | 13.33 | 13.83 | 13.83 | 13.74 | 13.75 | 14.13 | 16.17 | 14.14 | 12.50 | 11.96 | 13.36 | 13.23 | 14.11 | 14.28 | |
| Sr/Y | 30.94 | 28.21 | 32.73 | 39.99 | 39.46 | 43.22 | 33.81 | 38.21 | 48.61 | 164.46 | 141.36 | 93.10 | 107.11 | 106.57 | 120.05 | 88.68 | 83.57 | |
| La/Yb | 29.42 | 25.19 | 24.81 | 28.78 | 27.26 | 32.35 | 28.41 | 31.61 | 31.51 | 43.74 | 42.90 | 30.79 | 32.69 | 46.26 | 44.86 | 27.52 | 45.89 | |
| T _{Zr} (°C) | | | | | | | | | | 742.8 | 739.5 | 731.0 | 735.5 | 752.2 | 750.4 | 738.5 | 759.1 | |

Note: Eu/Eu* = 2*Eu_n/(Sm_n + Gd_n) using concentrations normalized to chondrite; T_{Zr} is the zircon saturation temperature (Watson and Harrison, 1983).

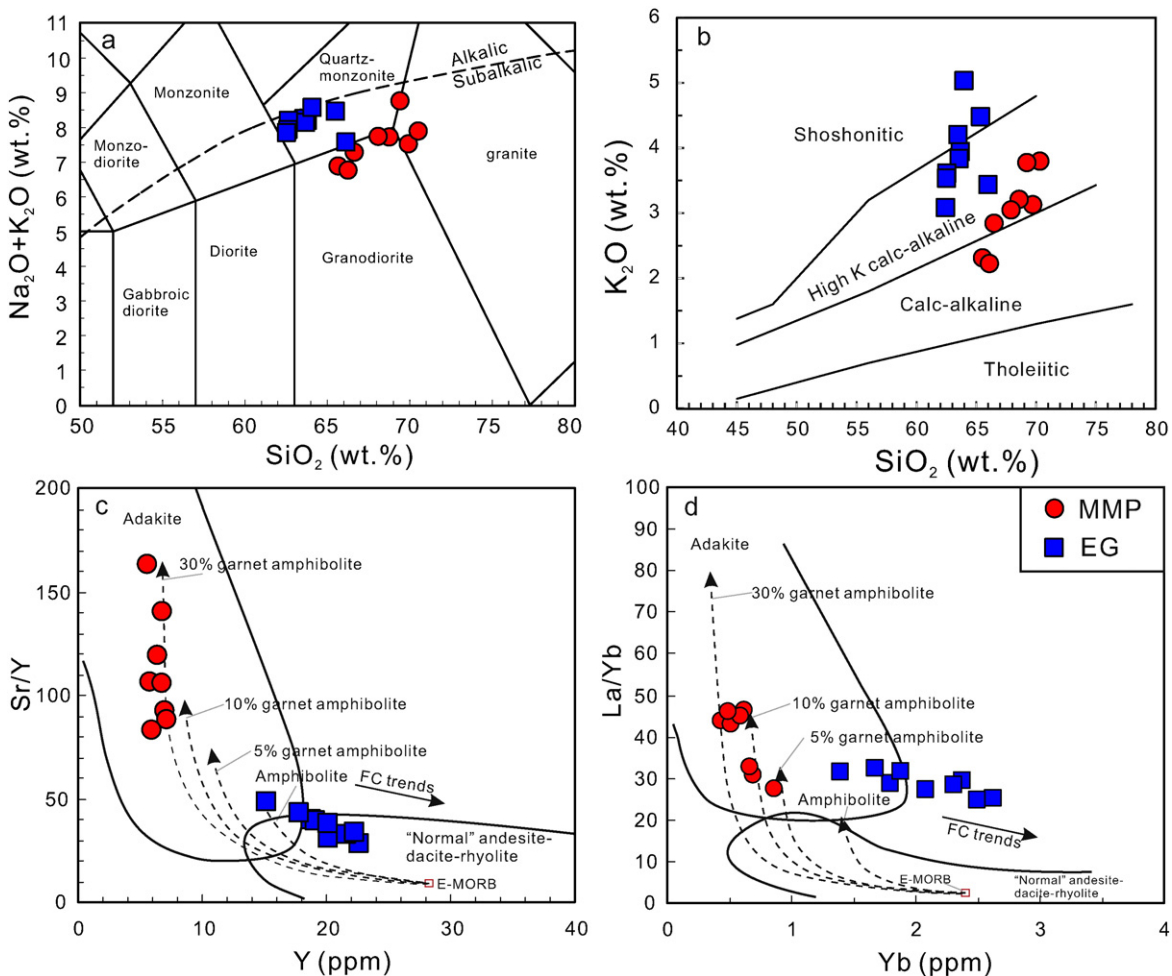


Fig. 6. Plots: (a) total alkalis-silica (TAS) diagram (Middlemost, 1994); (b) K_2O vs SiO_2 (Peccerillo and Taylor, 1976); (c) Sr/Y vs Y (Defant and Drummond, 1993); and (d) La/Yb vs Yb ($Castillo$ et al., 1999). Enriched-Mid oceanic Ridge Basalt (E-MORB) source from Sun and McDonough (1989). The simulated results of variable degrees of partial melting of different basaltic lower crust from Haschke et al. (2010) and Shafei et al. (2009).

slightly negative Eu anomaly (0.76–0.83) (Fig. 7a). The Eu anomaly and low Sr contents of 623–769 ppm may reflect that plagioclase removal playing a significant role in their genesis, while the moderate HREE fractionation precludes the retention of garnet in the restite. EG exhibits variable enrichment in large lithophile elements (LILEs; e.g., Rb, Ba, Th, U, K, Pb) and strong depletion of high-field strength elements (HFSEs; e.g., Nb, Ta, Ti), as shown on the primitive mantle-normalized spidergram

(Fig. 7b). Furthermore, EG generally has higher total REE and trace element contents than MMP (Fig. 7).

5.3. Whole-rock Sr-Nd and zircon Hf isotopes

The measured and age-corrected Sr-Nd isotopic compositions of EG and MMP are given in Table 3 and plotted on Fig. 8. The MMP has a

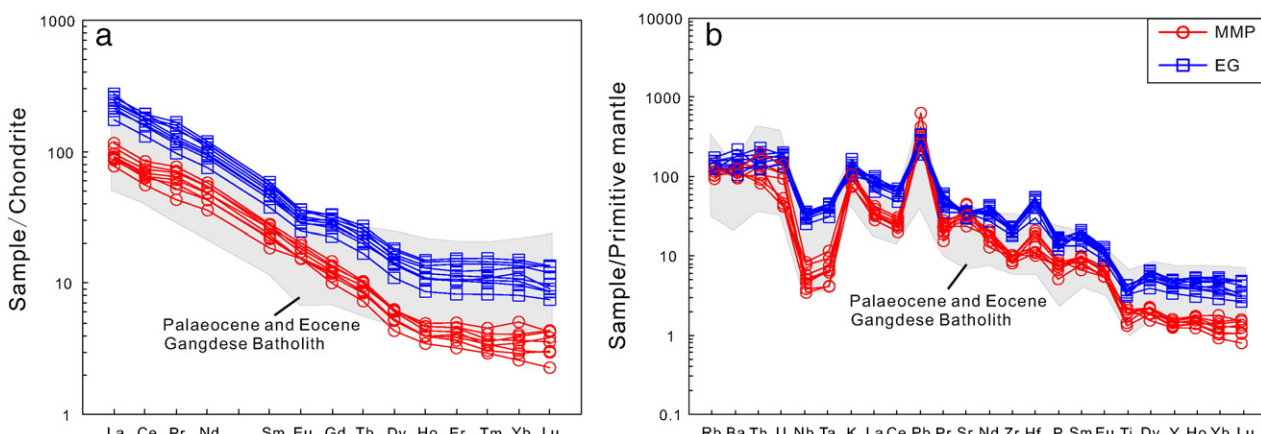


Fig. 7. Chondrite-normalized REE patterns (a) and primitive mantle-normalized trace element patterns (b) of EG and MMP at the Dabu deposit. Published data of the Palaeocene and Eocene Gangdese Batholith from Wen (2007) and Ji et al. (2012). Values for the chondrite and primitive mantle are from Sun and McDonough (1989).

Table 3
Sr–Nd isotopic data for EG and MMP at the Dabu porphyry deposit.

| Sample | Rock type | Rb | Sr | $^{87}\text{Rb}/^{86}\text{Sr}$ | $^{87}\text{Sr}/^{86}\text{Sr}$ | 26 | $^{87}\text{Sr}/^{86}\text{Sr}_{(i)}$ | Sm | Nd | $^{147}\text{Sm}/^{144}\text{Nd}$ | $^{143}\text{Nd}/^{144}\text{Nd}$ | 26 | $^{143}\text{Nd}/^{144}\text{Nd}_{(i)}$ | $\varepsilon\text{Nd}(t)$ | $T_{\text{DM}}(\text{Ma})$ |
|-----------|-----------|--------|--------|---------------------------------|---------------------------------|----------|---------------------------------------|------|-------|-----------------------------------|-----------------------------------|----------|---|---------------------------|----------------------------|
| DB11-35 | EG | 79.326 | 622.89 | 0.368383 | 0.705597 | 0.000005 | 0.705356 | 8.29 | 52.90 | 0.094762 | 0.512569 | 0.000006 | 0.512540 | -0.75 | 910 |
| DB11-36 | EG | 85.977 | 638.37 | 0.389590 | 0.705636 | 0.000004 | 0.705381 | 9.34 | 58.88 | 0.095888 | 0.512582 | 0.000007 | 0.512553 | -0.50 | 617 |
| DB11-76 | EG | 79.308 | 706.68 | 0.324654 | 0.705702 | 0.000005 | 0.705490 | 8.86 | 56.29 | 0.095188 | 0.51259 | 0.000005 | 0.512561 | -0.34 | 734 |
| DB11-75 | EG | 95.56 | 553.56 | 0.499350 | 0.705632 | 0.000005 | 0.705306 | 6.63 | 42.23 | 0.094856 | 0.512578 | 0.000006 | 0.512549 | -0.57 | 721 |
| DB11-29-1 | MMP | 86.958 | 785.34 | 0.320299 | 0.705799 | 0.000004 | 0.705733 | 4.60 | 25.88 | 0.107523 | 0.512487 | 0.000008 | 0.705733 | -2.78 | 552 |
| DB11-19 | MMP | 93.19 | 625.1 | 0.431243 | 0.705742 | 0.000005 | 0.705653 | 3.81 | 22.15 | 0.103986 | 0.512495 | 0.000008 | 0.512485 | -2.62 | 745 |
| DB11-74 | MMP | 113.3 | 643.53 | 0.509263 | 0.705238 | 0.000004 | 0.705135 | 3.91 | 25.06 | 0.094424 | 0.512668 | 0.000009 | 0.512659 | 0.77 | 735 |

Notes: $(^{87}\text{Sr}/^{86}\text{Sr})_i = (^{87}\text{Sr}/^{86}\text{Sr}) - (^{87}\text{Rb}/^{86}\text{Sr})(e^{\lambda t} - 1)$, $\lambda_{\text{Nb}} = 1.42 \times 10^{-11}/\text{year}^{-1}$; $(^{143}\text{Nd}/^{144}\text{Nd})_i = (^{143}\text{Nd}/^{144}\text{Nd}) - (^{143}\text{Nd}/^{144}\text{Nd})_{\text{CHUR}} = 6.54 \times 10^{-12}/\text{year}^{-1}$, $\lambda_{\text{Sm}} = 6.54 \times 10^{-12}/\text{year}^{-1}$, $\lambda_{\text{Nd}} = 0.1967$, $^{143}\text{Nd}/^{144}\text{Nd}_{\text{CHUR}} = 0.512638$, $^{147}\text{Sm}/^{144}\text{Nd}_{\text{DM}} = 0.51315$, $^{147}\text{Sm}/^{144}\text{Nd}_{\text{DM}} = 0.51315$, $^{143}\text{Nd}/^{144}\text{Nd}_{\text{DM}} = 0.2137$.

limited range of isotopic compositions, with $^{87}\text{Sr}/^{86}\text{Sr}_{(i)}$ ratios between 0.70514 and 0.70573, $\varepsilon\text{Nd}(t)$ between -2.78 and 0.77, and T_{DM} between 952 and 735 Ma. The EG displays a similar Sr–Nd isotopic range with $^{87}\text{Sr}/^{86}\text{Sr}_{(i)}$ ratios of 0.70531 to 0.70549, $\varepsilon\text{Nd}(t)$ values of -0.75 to -0.34, and model ages of 910 to 617 Ma.

In-situ Hf isotopic compositions of zircons from EG and MMP are listed in Table 4 and plotted on Fig. 9. Zircons from EG have initial $^{176}\text{Hf}/^{177}\text{Hf}$ ratios of 0.282842–0.282917, $\varepsilon\text{Hf}(t)$ values of 3.46–6.13 ($n = 12$), and T_{DM}^{C} ages between 901 and 731 Ma. Zircons from MMP have initial $^{176}\text{Hf}/^{177}\text{Hf}$ ratios of 0.282873 to 0.283013, $\varepsilon\text{Hf}(t)$ values of 3.82 to 8.85 ($n = 13$), and Hf isotope crustal model ages (T_{DM}^{C}) between 851 and 532 Ma. Both the positive $\varepsilon\text{Hf}(t)$ values and the distinctly young T_{DM}^{C} (Hf) ages for MMP and EG indicate a significant mantle input (e.g. Ma et al., 2013).

5.4. Zircon trace elements

Zircon trace element concentrations for EG and MMP are presented in Supplementary Table 1, and the chondrite-normalized REE zircon patterns are shown in Fig. 10a. Both the MMP and EG have similar REE patterns characteristic for magmatic zircons, such as positive Ce and negative Eu anomalies and HREE enrichment relative to LREE (Fig. 10a; Hoskin and Schaltegger, 2003). The method proposed by Ballard et al. (2002) is used here to estimate the magmatic oxygen fugacity, by which zircon $\text{Ce}^{4+}/\text{Ce}^{3+}$ ratios are calculated based on a lattice-strain model for mineral–melt partitioning of Ce^{4+} and Ce^{3+} cations, and trace elements in whole rock samples have also been used as a proxy for melt. The calculated $\text{Ce}^{4+}/\text{Ce}^{3+}$ of 58 to 164 and Eu/Eu^* ratios of 0.34 to 0.56 for zircons from EG are lower than the calculated $\text{Ce}^{4+}/\text{Ce}^{3+}$ of 87 to 1112 and Eu/Eu^* ratios of 0.45 to 0.72 for zircons from MMP (Fig. 10b).

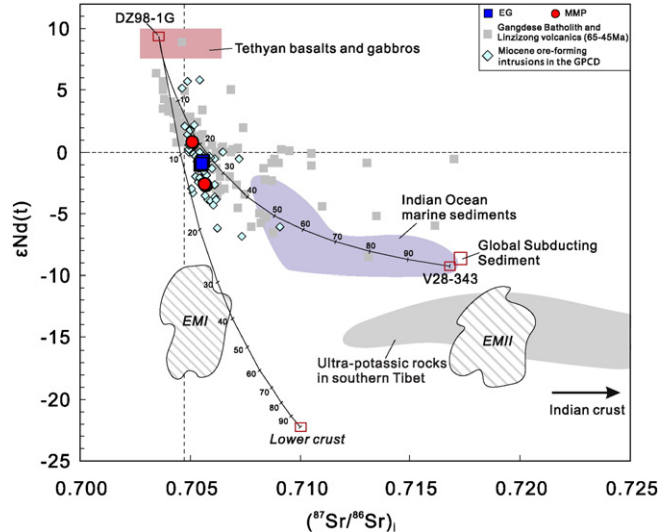


Fig. 8. $(^{87}\text{Sr}/^{86}\text{Sr})_i$ vs $\varepsilon\text{Nd}(t)$ diagram for EG and MMP at the Dabu deposit. Data sources for: Tethyan basalts and gabbros (including sample DZ98-1G from the Yarlung Zangbo suture zone; Zhang et al., 2005); Indian Ocean marine sediments (including sample V28-343 used as a proxy for Neo-Tethyan sediment; Ben Othman et al., 1989); global subducting sediment (Plank and Langmuir, 1998); ultra-potassic rocks (Miller et al., 1999; Gao et al., 2007; Zhao et al., 2009; Liu et al., 2014; Wang et al., 2014a); Miocene mineralization-related intrusions in the Gangdese porphyry copper deposits (Qu et al., 2004; Meng, 2004; Yang, 2008; Leng et al., 2013; Wang et al., 2006; Li et al., 2011; Zheng et al., 2014b; Hu et al., 2015); Gangdese Batholith and Linzizong volcanics (Mo et al., 2007, 2008; Wen, 2007; Lee et al., 2012); the lower crust (Miller et al., 1999); and the field of EMI and EMII (Zindler and Hart, 1986). All of the Sr–Nd isotopic data were recalculated at 15 Ma for comparison, except for the Indian Ocean marine sediments.

Table 4

Hf isotopic data for zircons from EG and MMP at the Dabu porphyry deposit.

| Spot | $^{176}\text{Yb}/^{177}\text{Hf}$ | 1σ | $^{176}\text{Hf}/^{177}\text{Hf}$ | 1σ | $^{176}\text{Lu}/^{177}\text{Hf}$ | 1σ | Age (Ma) | $\epsilon\text{Hf}(0)$ | $\epsilon\text{Hf}(t)$ | T_{DM} (Ma) | $f_{\text{Lu/Hf}}$ | T_{DM}^{C} (Ma) |
|----------------------|-----------------------------------|----------|-----------------------------------|----------|-----------------------------------|----------|----------|------------------------|------------------------|----------------------|--------------------|---------------------------------|
| <i>DB-75 for EG</i> | | | | | | | | | | | | |
| 1.1 | 0.011147 | 0.000731 | 0.282865 | 0.000011 | 0.000365 | 0.000026 | 45.0 | 3.3 | 4.28 | 539 | -0.99 | 848 |
| 2.1 | 0.044185 | 0.001169 | 0.282917 | 0.000010 | 0.001196 | 0.000025 | 47.5 | 5.1 | 6.13 | 477 | -0.96 | 731 |
| 3.1 | 0.026413 | 0.000683 | 0.282867 | 0.000010 | 0.000912 | 0.000023 | 46.4 | 3.4 | 4.34 | 545 | -0.97 | 845 |
| 4.1 | 0.035182 | 0.001109 | 0.282846 | 0.000009 | 0.000933 | 0.000029 | 49.2 | 2.6 | 3.65 | 575 | -0.97 | 891 |
| 5.1 | 0.021272 | 0.000832 | 0.282880 | 0.000010 | 0.000615 | 0.000020 | 47.0 | 3.8 | 4.84 | 521 | -0.98 | 813 |
| 6.1 | 0.073546 | 0.005122 | 0.282843 | 0.000012 | 0.001826 | 0.000130 | 46.2 | 2.5 | 3.46 | 593 | -0.94 | 901 |
| 7.1 | 0.046097 | 0.001337 | 0.282879 | 0.000009 | 0.001384 | 0.000043 | 43.5 | 3.8 | 4.71 | 534 | -0.96 | 819 |
| 8.1 | 0.057840 | 0.002046 | 0.282912 | 0.000010 | 0.001536 | 0.000055 | 45.9 | 4.9 | 5.90 | 489 | -0.95 | 744 |
| 9.1 | 0.080292 | 0.004290 | 0.282879 | 0.000009 | 0.001980 | 0.000106 | 46.5 | 3.8 | 4.75 | 543 | -0.94 | 819 |
| 10.1 | 0.030519 | 0.002301 | 0.282877 | 0.000009 | 0.001240 | 0.000131 | 46.2 | 3.7 | 4.69 | 535 | -0.96 | 822 |
| 11.1 | 0.052849 | 0.000679 | 0.282879 | 0.000011 | 0.001343 | 0.000019 | 44.3 | 3.8 | 4.73 | 533 | -0.96 | 818 |
| 12.1 | 0.051654 | 0.001332 | 0.282842 | 0.000010 | 0.001374 | 0.000020 | 46.2 | 2.5 | 3.46 | 587 | -0.96 | 901 |
| <i>DB-18 for MMP</i> | | | | | | | | | | | | |
| 1.1 | 0.000461 | 0.000006 | 0.017911 | 0.000271 | 0.282934 | 0.000012 | 14.4 | 5.7 | 6.03 | 445 | -0.99 | 712 |
| 2.1 | 0.000415 | 0.000024 | 0.016931 | 0.001077 | 0.282907 | 0.000012 | 15.0 | 4.8 | 5.09 | 482 | -0.99 | 773 |
| 3.1 | 0.000556 | 0.000012 | 0.021456 | 0.000419 | 0.282931 | 0.000012 | 12.1 | 5.6 | 5.89 | 449 | -0.98 | 719 |
| 4.1 | 0.000351 | 0.000006 | 0.013959 | 0.000281 | 0.282938 | 0.000009 | 17.8 | 5.9 | 6.27 | 437 | -0.99 | 699 |
| 5.1 | 0.001043 | 0.000024 | 0.039550 | 0.001012 | 0.282866 | 0.000010 | 46.4 | 3.3 | 4.31 | 548 | -0.97 | 847 |
| 6.1 | 0.000649 | 0.000005 | 0.025649 | 0.000337 | 0.282873 | 0.000009 | 10.8 | 3.6 | 3.82 | 532 | -0.98 | 851 |
| 7.1 | 0.000475 | 0.000010 | 0.017461 | 0.000363 | 0.283013 | 0.000009 | 15.6 | 8.5 | 8.85 | 334 | -0.99 | 532 |
| 8.1 | 0.000390 | 0.000005 | 0.015513 | 0.000177 | 0.282915 | 0.000009 | 15.7 | 5.0 | 5.39 | 470 | -0.99 | 754 |
| 9.1 | 0.000424 | 0.000008 | 0.016295 | 0.000196 | 0.282940 | 0.000010 | 16.3 | 5.9 | 6.29 | 436 | -0.99 | 697 |
| 10.1 | 0.000649 | 0.000020 | 0.024904 | 0.000849 | 0.283010 | 0.000009 | 16.8 | 8.4 | 8.77 | 340 | -0.98 | 538 |
| 11.1 | 0.000616 | 0.000011 | 0.022092 | 0.000422 | 0.282967 | 0.000011 | 14.7 | 6.9 | 7.20 | 400 | -0.98 | 637 |
| 12.1 | 0.000489 | 0.000031 | 0.020163 | 0.001426 | 0.282961 | 0.000009 | 16.0 | 6.7 | 7.04 | 406 | -0.99 | 648 |
| 13.1 | 0.000406 | 0.000005 | 0.015431 | 0.000203 | 0.282918 | 0.000009 | 13.4 | 5.2 | 5.46 | 466 | -0.99 | 748 |
| 14.1 | 0.000538 | 0.000011 | 0.019100 | 0.000302 | 0.282958 | 0.000009 | 14.5 | 6.6 | 6.89 | 412 | -0.98 | 657 |

5.5. Mineral chemistry

The compositions of biotite, apatite, magnetite, and ilmenite from EG and MMP are listed in Supplementary Table 2. The biotite has a similar Mg number (i.e. $\text{Mg}/(\text{Mg} + \text{Fe}_{\text{Ti}})$) between 0.58 and 0.76 and overlaps with the range of magnesium biotite (Fig. 11a). The calculated $\text{Fe}^{3+}/\text{Fe}^{2+}$ ratios for biotite from MMP range from 0.11 to 0.38 and between 0.05 and 0.22 from EG. The Ti concentrations for biotite from MMP are markedly higher (0.25–0.44) than those in EG (0.04–0.05) (Fig. 11c). In addition, MMP samples plot at higher temperatures than samples from EG on the Ti versus $\text{Mg}/(\text{Mg} + \text{Fe})$ diagram (Fig. 11d; Henry, 2005). The F (2.66–3.72%) and Cl (0.06–0.53%) contents for apatite in MMP are also higher than those in EG (0.85–1.50%, 0.02–0.03%, respectively) (Fig. 10c). The magmatic oxidation states are estimated by the magnetite–ilmenite mineral pairs based on the ILMAT spreadsheet of Lepage (2003). The representative magnetite–ilmenite pairs from MMP yielded calculated temperature of 633 °C and LogfO_2 value of -14, which is higher than the temperature of 553 °C and LogfO_2 value of -22 for EG (Fig. 10d).

6. Discussion

6.1. Origin of the EG and MMP

The EG has a relatively flat MREE–HREE pattern and a small negative Eu anomaly, does not have a concave-upward chondrite-normalized REE pattern, and is geochemically similar to the Palaeocene–Eocene Gangdese Batholith that formed from melts generated by the partial melting of either a newly underplated basaltic lower crust or subduction-modified lithospheric mantle (Fig. 7a; Wen, 2007; Ji et al., 2012). These features provide evidence supporting the involvement of plagioclase instead of amphibole and garnet as either a fractionated phase or residual mineral in the source region. The EG and published data for the Batholith have overall low Sm/Yb (generally <4) and high La/Sm (up to 13) ratios, suggesting a less LREE-enriched and pyroxene-dominated residual mineralogy (Fig. 13f; Kay and Mpodozis,

2001). The EG has low Sr/Y and La/Yb ratios that are consistent with generation from the crust with an inferred thickness of ~45 km (Fig. 6c, d; Hildreth and Moorath, 1988). In comparison, the MMP has high Sr/Y (84–164) and La/Yb (28–46) ratios, low Y (5.56–7.11 ppm) and Yb (0.44–0.87 ppm) concentrations, and strongly fractionated REE patterns with a negative HREE slope, all of which are indicative of derivation from a thickened source region dominated by amphibole and garnet fractionation or restite equilibration (Figs. 6c, d, and 7a).

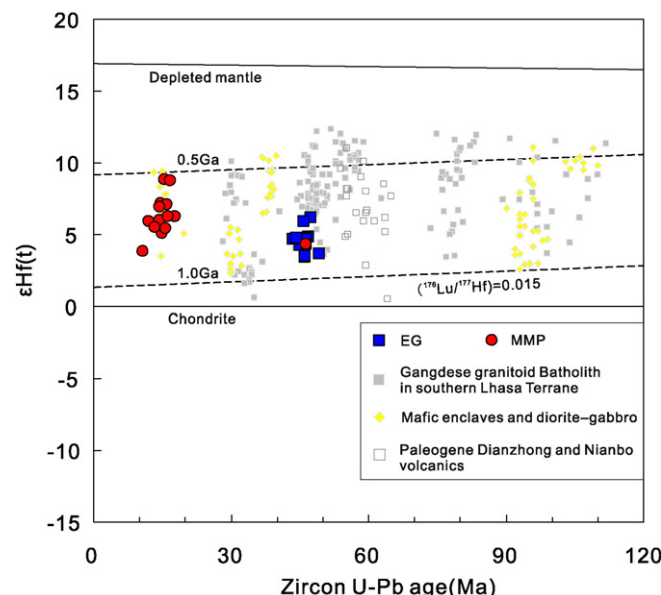


Fig. 9. Plot of $\epsilon\text{Hf}(t)$ values vs U-Pb ages of zircons from EG and MMP at the Dabu deposit. Data of the Gangdese Batholith in the southern Lhasa Terrane from Du et al. (2012), Ma et al. (2014), and Chen et al. (2015); mafic enclaves and diorite–gabbro from Guan et al. (2012), Zheng et al. (2012b, 2014a), Ma et al. (2013) and Wu et al. (2014); Palaeogene Linzizong (Dianzhong and Nianbo) volcanics from Lee et al. (2007).

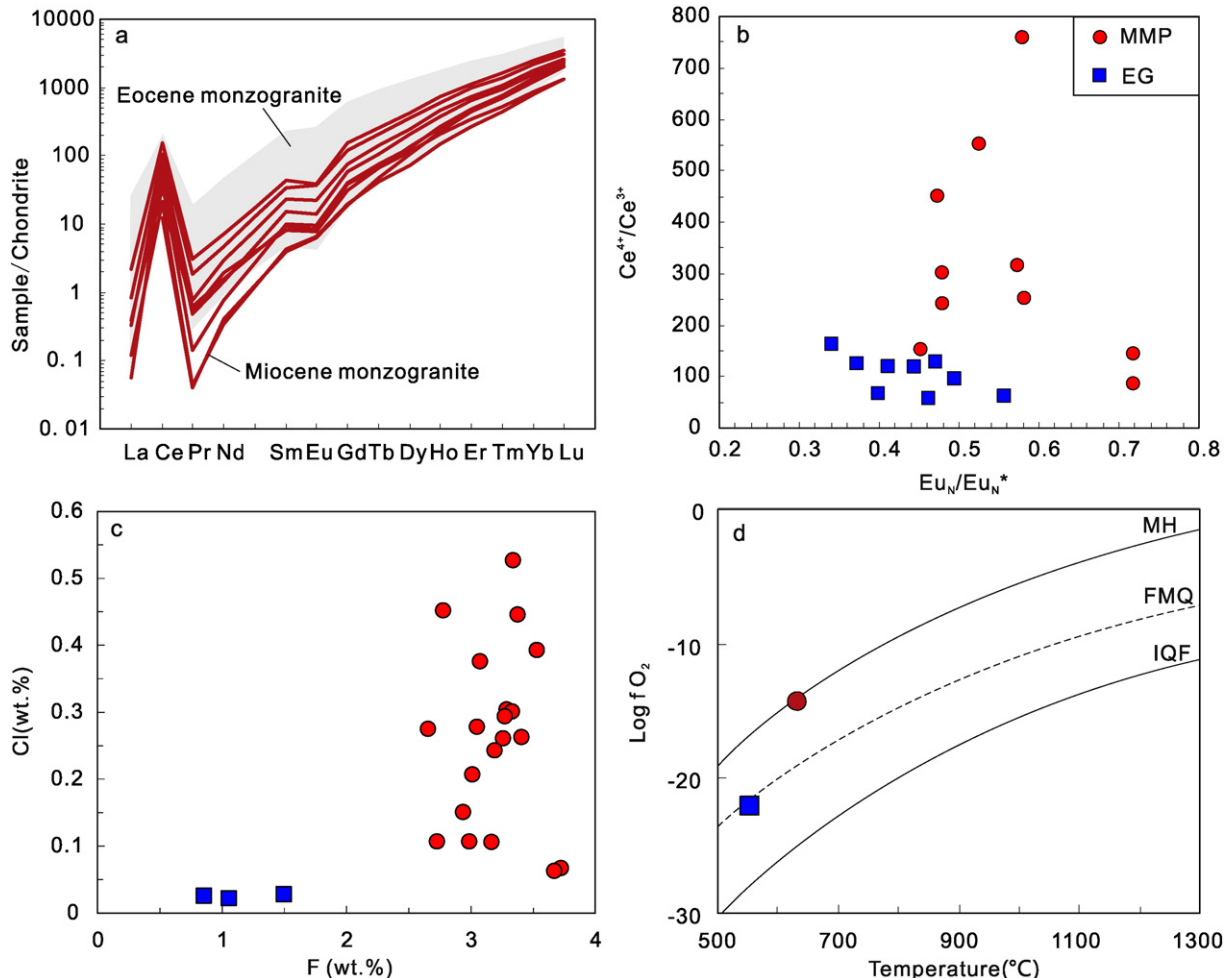


Fig. 10. Plots: (a) Chondrite-normalized trace element diagram for zircons; (b) zircon Ce⁴⁺/Ce³⁺ vs Eu_N/Eu_{N*}, (c) Cl vs F for apatite; and (d) log fO₂ vs temperature estimated from magnetite-ilmenite mineral pairs (Lattard et al., 2005) from EG and MMP at the Dabu deposit. Abbreviations: HM = hematite–magnetite buffer curve, FMQ = fayalite–magnetite–quartz buffer curve, IQF = iron–quartz–fayalite buffer curve.

On the plot of Sm/Yb versus La/Sm (Fig. 13f), the MMP overlaps with the range of Miocene Cu-mineralization-related felsic rocks with high Sm/Yb ratios (4–10), which also reflect the presence of a thickened lower crust with amphibole and garnet in the source. A basaltic source composition extracted from an enriched upper mantle (E-MORB), as discussed by Sun and McDonough (1989), was used to model the variable degrees of partial melting of different basaltic lower crust dominated by garnet-bearing amphibolite source mineralogies on Sr/Y versus Y and La/Yb versus Yb diagrams (Fig. 6c, d). The results suggest that garnet-bearing (5–30%) amphibolite lower crust accounted for the parental magma for MMP, consistent with the overthickened crust of 70–80 km beneath the Lhasa Terrane (Kind et al., 1996; Chung et al., 2009).

The MMP has a limited range of isotopic compositions with $^{87}\text{Sr}/^{86}\text{Sr}_{(i)} = 0.70514\text{--}0.70573$, $\epsilon\text{Nd(t)} = -2.78\text{ to }0.77$, and $T_{\text{DM}} = 952\text{--}735$ Ma. These values are similar to those of Miocene mineralization-related intrusions within GPCD with $^{87}\text{Sr}/^{86}\text{Sr}_{(i)} = 0.70439\text{--}0.70594$, $\epsilon\text{Nd(t)} = -6.8\text{ to }5.9$ (Meng, 2004; Qu et al., 2004; Wang et al., 2006; Yang, 2008; Li et al., 2011; Leng et al., 2013; Zheng et al., 2014b; Hu et al., 2015). The EG has a Sr–Nd isotopic range similar to MMP, with $^{87}\text{Sr}/^{86}\text{Sr}_{(i)}$ values of 0.70531–0.70549, $\epsilon\text{Nd(t)}$ values of $-0.75\text{ to }-0.34$, and model ages of 910–617 Ma. The Sr–Nd isotopic compositions of MMP and EG fall within the range of the 65–45 Ma Gangdese Batholith and Linzizong volcanics, both of which are thought to have formed from arc magma sourced from a mantle wedge that was metasomatized by slab-derived fluids or sediment-derived melts during the Neo-Tethyan Ocean subduction (Mo et al., 2007, 2008; Wen, 2007;

Lee et al., 2012). On passing, the initial ϵNd values and $^{87}\text{Sr}/^{86}\text{Sr}$ ratios of all of the samples in Fig. 8 were recalculated as $T = 15$ Ma.

There is no difference in zircon Hf isotopic compositions between Palaeogene and Miocene rocks when plotted on an age versus $\epsilon\text{Hf(t)}$ diagram (Fig. 9), with both MMP and EG plotting in the evolution field of Cretaceous, Palaeocene–Eocene, and Oligocene–Miocene igneous rocks such as granitic rocks, mafic enclaves, diorite–gabbro intrusions, and volcanics (Lee et al., 2007; Du et al., 2012; Guan et al., 2012; Zheng et al., 2012b, 2014a; Ma et al., 2013, 2014; Wu et al., 2014; Chen et al., 2015). The fact that the Sr–Nd–Hf isotopic compositions of MMP and EG are indistinguishable suggests that they have a common magma source, although their REE and spider patterns are distinctively different.

Both MMP and EG are significantly enriched in LILEs (Ba, Rb, K, and Sr), but are depleted in HFSEs (Nb, Ta, and Ti) and have positive Pb anomalies when compared to the composition of the primitive mantle (Fig. 7b). These characteristics are indicative of subduction-related arc magmas (e.g. Tatsumi et al., 1986; Pearce and Parkinson, 1993; Elburg et al., 2002). Generally, slab-derived aqueous fluids contain low concentrations of REEs, Th and HFSEs, but can introduce significant amounts of LILEs and other fluid-mobile trace elements such as U and Pb into a mantle wedge. In comparison, partial melts derived from subducted continental sediments are characterized by relatively high Th and LREE concentrations (Guo et al., 2013 and references therein). Consequently, high Ba/La, Ba/Th, Rb/Y, Sr/Th, and Sr/Nd ratios are generally thought to be indicative of arc magma derived from sources that had

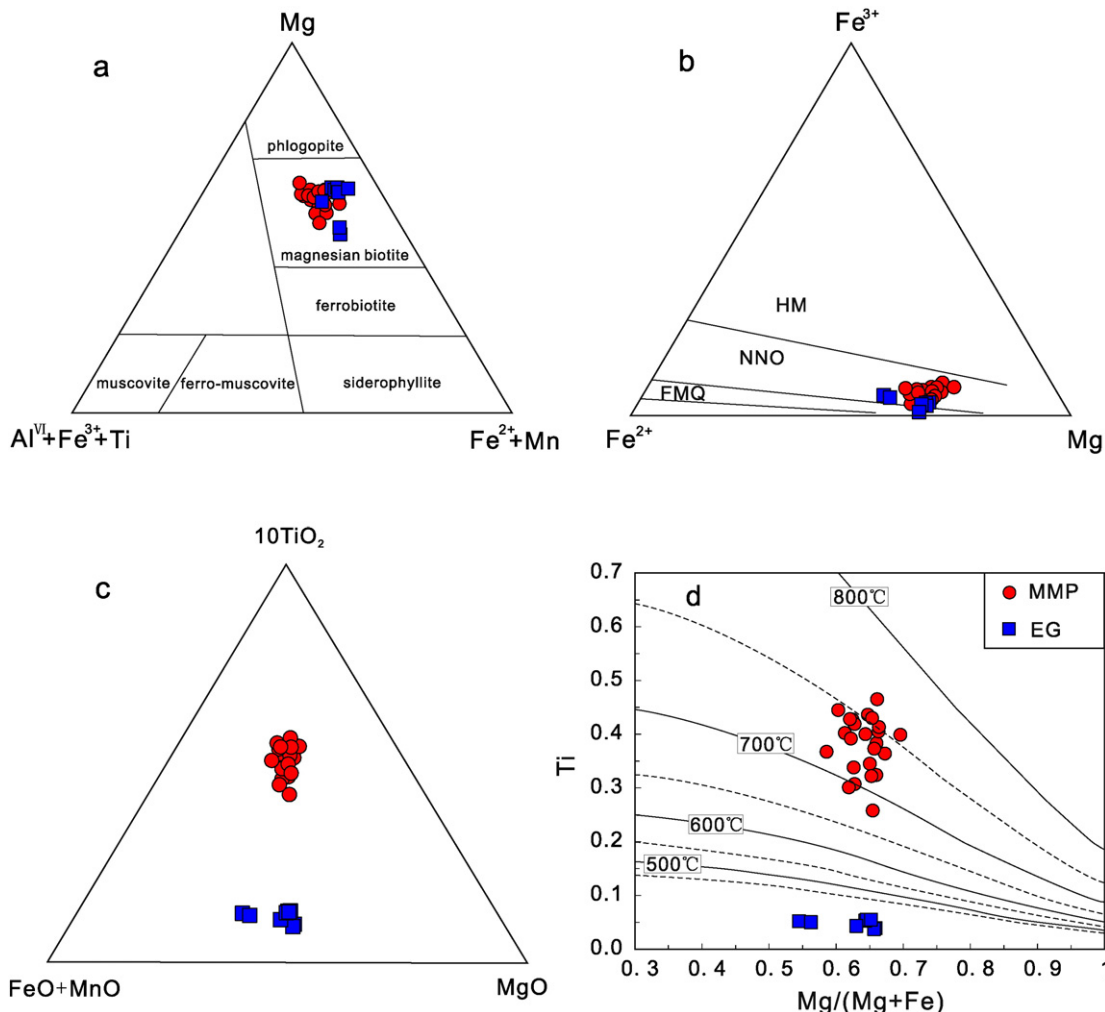


Fig. 11. Plots: (a) Mg–(Al^{VII} + Fe³⁺ + Ti)–(Fe²⁺ + Mn) (Foster, 1960); (b) Fe³⁺–Fe²⁺–Mg (Wones and Eugster, 1965); (c) 10TiO₂–(FeO + MnO)–MgO; and (d) Ti vs Mg/(Mg + Fe) (Henry, 2005) for biotite from EG and MMP at the Dabu deposit. Abbreviations: HM = hematite–magnetite oxygen buffer, NNO = Ni + NiO oxygen buffer, FMQ = fayalite–magnetite–quartz oxygen buffer.

been strongly metasomatized by a fluid component, whereas rocks with sources that had been enriched by partial melts derived from subducted continental sediments are likely to have high Th/Yb, Th/Pb, and Th/Nb ratios. The EG, MMP, Gangdese Batholith, and Miocene mineralization-related intrusions within GBCD have variable Sr/Th, Sr/Nd, Ba/Th, and Rb/Y ratios, but narrow ranges of Th concentrations and Th/Yb, Th/Nb, and Th/Pb ratios; these characteristics are consistent with derivation from a magma that underwent subducted slab-derived fluid-related enrichment (Fig. 12; Meng, 2004; Qu et al., 2004; Wang et al., 2006; Yang, 2008; Li et al., 2011; Ji et al., 2012; Leng et al., 2013; Zheng et al., 2014b; Hu et al., 2015). In contrast, Miocene ultra-potassic rocks define a different source enrichment trend, with high Th/Yb, Th/Nb, and Th/Pb ratios reflecting derivation from magma associated with enrichment related to subducted continental sediments (Fig. 12; Miller et al., 1999; Gao et al., 2007; Wen, 2007; Zhao et al., 2009; Liu et al., 2014; Wang et al., 2014a).

The MMP and EG also share a distinct Sr–Nd isotopic range with co-eval ultra-potassic volcanics that were derived from an enriched lithospheric mantle that had been metasomatized by subducted Indian continental material resulting in magma that is less hydrous and formed under less oxidized conditions (Fig. 8; Ding et al., 2003; Zhao et al., 2009; Wang et al., 2014d). Instead, MMP and EG, as well as the Gangdese Batholith and Miocene mineralization-related intrusions, fall on a mixing line between the Tethyan basalts and Indian Ocean pelagic sediments, indicating derivation from a magma sourced from regions of

the mantle that underwent differing amounts of interaction with subducted oceanic sediments (Fig. 8). These geochemical data, combined with the fact that the occurrence of the Miocene GBCD defines a linear trend and is evenly spaced along the Yarlung Zangbo Suture, suggest a genetic link between earlier Neo-Tethyan subduction and the formation of both the MMP and Miocene mineralization-related porphyritic intrusions (Fig. 1b; Hou et al., 2009; Zheng et al., 2015).

It is here concluded that the transition from normal arc-magmatism during the Eocene to adakite-like high Sr/Y calc-alkaline magmatism in the Miocene dominated by entirely different mineral phases was due to a gradual increase in the crustal thickness and maturation of the arc (Fig. 13i; Jamali and Mehrabi, 2015). The EG was generated by partial melting of a basaltic source in the lower crust that was formed by newly underplating of subduction-modified lithospheric mantle-derived magma, which was subsequently fractionated crystallizing pyroxene and plagioclase. In comparison, MMP formed from the remelting of previously underplated basaltic melts at the base of the lower crust that had undergone post-collisional thickening and metamorphism to garnet-bearing amphibole facies.

6.2. Magmatic oxygen fugacity

The trace element composition of zircon is a sensitive indicator of the oxidation state of the magma in which it crystallized, because a zircon can incorporate multivalent Ce and Eu within its crystal structure,

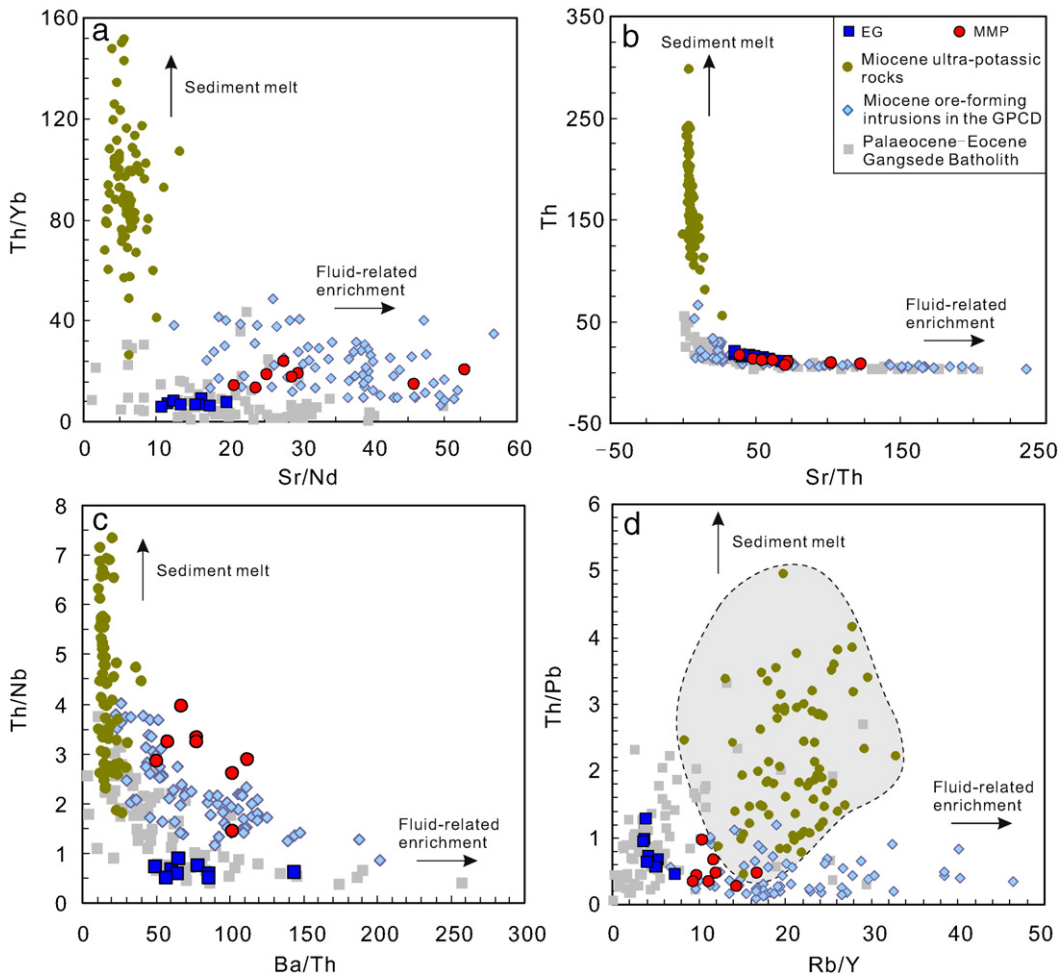


Fig. 12. Plots: (a) Th/Yb vs Sr/Nd, (b) Th vs Sr/Th, (c) Th/Nb vs Ba/Th, and (d) Th/Pb vs Rb/Y. Published data for the Miocene ore-forming intrusions in GPCB and ultra-potassic rocks are the same as in Fig. 8, and the data for the Gangdese Batholith are from Wen (2007) and Ji et al. (2012).

with oxidized Ce^{4+} preferentially incorporated into zircon relative to trivalent REEs. In contrast, reduced Eu^{2+} cannot be incorporated into a zircon. This means that a zircon with high $\text{Ce}^{4+}/\text{Ce}^{3+}$ and high $\text{Eu}_{\text{N}}/\text{Eu}_{\text{N}}^*$ ratios is indicative of high oxygen fugacity conditions and, as such, is characteristic of an intrusion that is a prospective host for porphyry Cu mineralization (Ballard et al., 2002; Hoskin and Schaltegger, 2003; Dilles, 2015). The zircon $\text{Ce}^{4+}/\text{Ce}^{3+}$ and $\text{Eu}_{\text{N}}/\text{Eu}_{\text{N}}^*$ ratios for MMP and EG have been calculated in this study following the example of Ballard et al. (2002). The results show that zircons within MMP have higher $\text{Ce}^{4+}/\text{Ce}^{3+}$ (87–1112) and $\text{Eu}_{\text{N}}/\text{Eu}_{\text{N}}^*$ (0.45–0.72) ratios than zircons in EG (58–164 and 0.34–0.56, respectively), implying increasing oxygen fugacity from the Eocene to the Miocene (Fig. 10b). Also estimated is the crystallization temperatures based on the Ti-in-zircon thermometer (Ferry and Watson, 2007) by setting the activities of SiO_2 to 1 and TiO_2 to 0.6. The average results show that MMP crystallized at 683 °C and EG crystallized at a similar temperature of 706 °C.

Fe-Ti oxide thermometry and oxybarometry are based on temperature- and redox-sensitive equilibria between titanomagnetite and ilmenite-hematite solid solutions, and these approaches have been widely used to provide information on the temperature and oxygen fugacity conditions during magmatic processes (e.g. Buddington and Lindsley, 1964; Lattard et al., 2005; Sauerzapf et al., 2008). Magnetite-ilmenite pairs and the ILMAT spreadsheet of Lepage (2003) were used to estimate the magmatic oxidation states. Pairs from EG yielded calculated temperature of 553 °C and ΔFMQ value (relative to the FMQ buffer at 1 kbar; O'Neill, 1987) of −0.3 and plot on the fayalite-magnetite-quartz (FMQ) oxygen buffer line (Fig. 10d). In comparison, MMP yielded

calculated temperature of 633 °C and ΔFMQ value of 5.0 and plot on the magnetite-hematite (MH) oxygen buffer line (Fig. 10d).

Biotite is a common mafic mineral in most felsic magmatic rocks and is structurally and chemically sensitive to the temperature, pressure, and oxygen fugacity of the host magma (e.g. Henry, 2005; Uchida et al., 2007; Shabani, 2010). The relative abundance of annite (Fe^{2+}) and oxyannite (Fe^{3+}) components in biotite can provide evidence for the redox conditions during the evolution of a felsic melt (Wones and Eugster, 1965). Biotite in MMP is stable in conditions between the Ni-NiO (NNO) and $\text{Fe}_3\text{O}_4-\text{Fe}_2\text{O}_3$ (HM) buffers, which suggests an evolutionary oxidizing trend that is responsible for the increasing oxyannite component (Fig. 11b). Most of the biotite from EG plots close to the NNO buffer, indicating a lower magmatic oxygen fugacity than during the formation of MMP (Fig. 11b). All of the above evidence indicates that the fertile MMP formed under higher oxygen fugacity conditions than the barren EG.

Arc magma formed above subduction zones is generally highly oxidized (Brandon and Draper, 1996; Parkinson and Arculus, 1999; Frost and McCammon, 2008; Kelley and Cottrell, 2009; Mullen and McCallum, 2013). The addition of oxidized components such as Fe^{3+} or dissolved sulfate is derived from dehydration or partial melting of subducting oceanic plates and overlying sediments. This is thought to be a major mechanism for the oxidation of arc magma during the interaction with fluids or melts (Wood et al., 1990; Kelley and Cottrell, 2009; Rowe et al., 2009).

Lécuyer and Ricard (1999) suggest that the transfer of ferric iron from magnetite produced during the hydrothermal alteration of oceanic

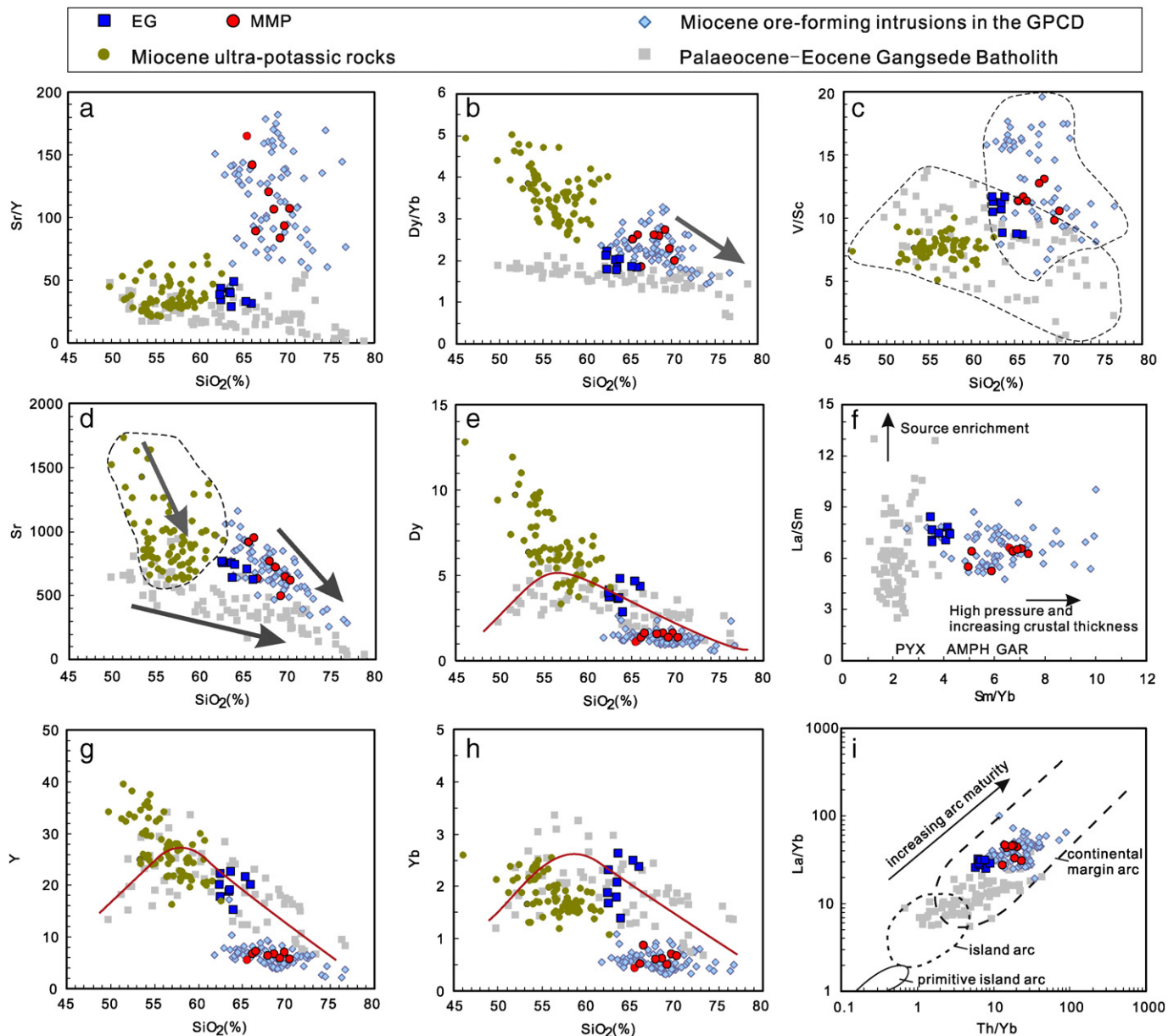


Fig. 13. Geochemical correlation diagrams for EG and MMP at the Dabu deposit, and published data of Miocene mineralization-related intrusions in GPCB, ultra-potassic rocks, and Gangdese Batholith. Data sources are the same as for Fig. 12. The approximate boundaries in the La/Sm vs Sm/Yb diagram are from Kay and Mpodozis (2001). The plot of La/Yb vs Th/Yb is after Condie (1989). Abbreviations: AMPH = amphibole, GAR = garnet, PYX = pyroxene.

crust towards the mantle is the main process responsible for the oxidized nature of arc magma. Lee et al. (2010), however, suggest that the highly oxidized nature of arc lava must be, at least in part, a consequence of shallow-level differentiation processes rather than solely reflecting the nature of the magma source. In any case, it is clear that arc magma that forms in subduction zones is generally oxidized.

As discussed in Section 6.1, MMP and EG exhibit magmatic arc geochemical characteristics and share a common magma source that had been metasomatized by subducting slab-derived fluid and oceanic sediments. It is also clear that the fertile MMP formed under higher magmatic oxygen fugacity than the barren EG. The question therefore remains as to which key factors or processes reduced the magmatic oxygen fugacity for EG?

Previous research has suggested several processes that might lower oxygen fugacity during the evolution of a magma, including (1) the degassing of oxidized volatile species (i.e. CO_2 , SO_3 , and SO_2), thereby lowering the amount of oxygen in the magma or reducing sulfate to sulfide (Oyarzun et al., 2001; Kelley and Cottrell, 2012); (2) the

assimilation of subducted continental crust, organic-rich sediments, or wall rocks during magma ascent (Shen and Pan, 2013; Wang et al., 2014d); and (3) the fractional crystallization of magnetite and hematite, thereby lowering the abundance of ferric iron in the magma (Sun et al., 2004, 2013a). The Gangdese Batholith and the coeval Linzizong volcanics are widespread throughout the Lhasa Terrane cropping out over an area of $\sim 1000 \times 200$ km (Fig. 1b; Wen, 2007; Mo et al., 2008; Ji et al., 2009; Lee et al., 2009). In addition, the ca. 50 Ma magmatic ‘flare-up’ is recorded by the Linzizong volcanism represented by the Pana Formation. The volcanism is characterized by significant geochemical variations from low-K tholeiitic through calc-alkaline to shoshonitic compositions, which suggests heterogeneous mantle and crustal sources (Lee et al., 2012). These features indicate that magma forming EG was generated in an open magmatic system (Oyarzun et al., 2001; Asadi et al., 2014). This was associated with the decompression and discharge of SO_2 during the Linzizong volcanism, a process that in turn reduced the oxygen fugacity in the EG magma. In comparison, the absence of volcanism under compressional conditions during the Miocene, as

documented by Zheng et al. (2007a), prevented the escape of volatiles from sulfur-rich and highly oxidized magma within the closed porphyry magma, which favored the formation of porphyry Cu mineralization. This model is further supported by the fact that apatite in MMP has higher volatile concentrations (e.g. F and Cl) than the apatite in EG (Fig. 10c).

6.3. Magmatic water content

Magmatic water (or fluid) plays a key role in the formation of porphyry Cu deposits (Richards, 2011a). However, directly measuring the content of magmatic water is difficult, primarily as a result of the extensive degassing of magma as it reaches the surface. Previous estimates of magmatic H₂O abundances are generally based on plagioclase hygrometer analysis and the analysis of undegassed basaltic glasses or melt inclusions (Walker et al., 2003; Kelley and Cottrell, 2009; Lange et al., 2009). Lu et al. (2015) introduced a geohyrometer for granites using zircon-saturation thermometry and H₂O-dependent phase equilibria, and concluded that the high Sr/Y copper ore-forming magma in the Gangdese porphyry Cu belt had dissolved H₂O contents of >10 wt.%. Furthermore, some whole-rock element ratios and the order of crystallization of minerals such as hornblende, feldspar, and magnetite can provide evidence of the water content of initial melts (Loucks, 2014; Wang et al., 2014c). For example, Sr can substitute for Ca in plagioclase under typical magmatic conditions and is therefore a sensitive indicator of plagioclase fractionation (McKay et al., 1994). Immobile elements such as V and Sc behave similarly during partial melting and are not perturbed by degassing, meaning that their abundances are generally unaffected by hydrothermal alteration (Canil, 1997; Anser Li and Aeolus Lee, 2004). In detail, the partitioning of the element V is redox-sensitive and has a very high magnetite–melt partition coefficient, whereas Sc partitions strongly into hornblende (La Tourrette et al., 1991; Sisson, 1994). Experimental studies have shown that the crystallization of hornblende from basaltic and basaltic–andesitic melt compositions above ~980 °C requires a melt containing >5 wt.% dissolved H₂O (Feig et al., 2006). If the bulk H₂O content of a silicate melt remains at 6 wt.% during differentiation, the crystallization sequence of minerals will be hornblende followed by plagioclase and finally magnetite. However, the crystallization of plagioclase prior to that of hornblende during cooling at any given pressure will be expected in a dry mafic-to-felsic differentiation series (Loucks, 2014 and references therein). This indicates that magmatic rocks with high V/Sc and Sr/Y ratios and high Sr concentrations most likely reflect the fractional crystallization of hornblende from more hydrous mafic melts. This process removes Y and Sc from the melt, but enriches the residual melt in Sr, Ti, and Fe³⁺ resulting in the suppression or delay of magnetite and plagioclase crystallization.

Both EG and Gangdese Batholith have low Sr/Y ratios of <50, relatively high Y and Yb values, and Sr concentrations that decrease over a wide range of SiO₂ contents from ~49 to 77 wt.% (Fig. 13a, d, g, h; Wen, 2007; Ji et al., 2012). These characteristics indicate that plagioclase fractionation proceeded throughout the evolution of the magma from mafic to felsic compositions. The Dy, Y, and Yb concentrations of these rocks rapidly increase at ~60 wt.% SiO₂ before subsequently decreasing at a higher silica content (Fig. 13e, g, h). This suggests that hornblende, which preferentially incorporates Dy as well as REEs (Moyen, 2009), did not begin to fractionate until the magma reached relatively evolved compositions. This view is consistent with the observation that the late-crystallized hornblende is generally present as small crystals within earlier formed feldspar phenocrysts in EG (Fig. 3e). The intrusions also have relatively low V/Sc ratios that gradually decrease with increasing SiO₂ as shown in Fig. 13c, which is indicative of magnetite fractionation being another process that can remove Fe³⁺ from a melt and contributed to the low magmatic oxygen fugacity of EG. All of these features suggest that the magma forming EG, as well as the rocks in the Palaeocene–Eocene Gangdese arc, were relatively dry with magmatic water contents of <4 wt.% (Ridolfi et al., 2009; Loucks, 2014). In contrast,

magma forming MMP at the Dabu deposit, as well as other Miocene mineralization-related intrusions in the GBCD, have high Sr/Y and V/Sc ratios, and low Dy and Y concentrations (Fig. 13a, c, e, g; Meng, 2004; Qu et al., 2004; Wang et al., 2006; Yang, 2008; Li et al., 2011; Leng et al., 2013; Zheng et al., 2014b; Hu et al., 2015). This suggests that the magma underwent early hornblende crystallization (Lu et al., 2015). The hornblende fractionation is also indicated by a negative correlation between Dy/Yb ratios and SiO₂ concentrations (Fig. 13b).

MMP also has a higher Sr concentration than EG and the Gangdese Batholith at constant SiO₂ values and records a rapid decrease in Sr concentrations with an increase in SiO₂ concentrations from 62 to 77 wt.% (Fig. 13d). These features may reflect the suppression of early plagioclase fractionation by hornblende crystallization resulting in high Sr concentrations, which is consistent with the absence of hornblende phenocrysts in the felsic MMP primarily because hornblende had already crystallized out from the hydrous mafic melt. All of this evidence indicates that the magma forming MMP was hydrous containing >5.5 wt.% magmatic water (Loucks, 2014). In addition, based on the geohyrometer introduced by Lu et al. (2015), the inferred H₂O content dissolved in MMP is ~11%, corresponding to zircon saturation temperatures of 731–759 °C.

The ultra-potassic rocks in the region have lower Sr/Y and V/Sc ratios that are comparable to the barren Gangdese Batholith (Fig. 13a, c; Miller et al., 1999; Gao et al., 2007; Zhao et al., 2009; Liu et al., 2014; Wang et al., 2014a). These rocks also have negative correlations between Dy/Yb ratios and Sr concentrations compared to SiO₂ contents (Fig. 13b, d). This indicates that both hornblende and plagioclase crystallized early from relatively hydrous melts. However, it is here suggested that the magma forming the Miocene mineralization-related intrusions was more hydrous than the magma forming the ultra-potassic rocks primarily because the former have lower Dy and Y concentrations than the latter (Fig. 13e, g). We therefore infer that the extremely high water content of >10% in MMP and the Miocene mineralization-related intrusions, as documented by Lu et al. (2015), is unlikely to be associated with ultra-potassic magma.

In running summary, the EG and ca. 65–45 Ma Gangdese Batholith formed from dry magma with <4% H₂O, which experienced plagioclase and magnetite fractionation, whereas the Miocene ultra-potassic rocks formed from relatively hydrous magma that fractionated both hornblende and plagioclase early during its magmatic history. MMP and other Miocene mineralization-related intrusions formed from even more hydrous magma with >5.5% H₂O, as shown by the early fractionation of hornblende and the suppression of plagioclase crystallization. As discussed in Section 6.1, both MMP and EG were derived from magma generated in a common source region that had been metasomatized by subducted slab-derived fluids and oceanic sediments. The question remains as to what happened from the Eocene to the Miocene to increase the magmatic water contents for the generation of ore-productive intrusions?

Porphyry Cu deposits formed in the post-collisional setting in southern Tibet are special because they experienced not only a long-lived northward subduction of the Neo-Tethyan ocean slab, but also the subsequent collision of the Indian and Asian plates accompanied by gradual crust thickening and shortening (Wen et al., 2008; Chung et al., 2009; Ji et al., 2009). During such processes, the mafic lower crust of the South Lhasa Terrane would have also experienced intense deformation and metamorphism as a result of increasing regional stress in the Himalaya–Tibet orogenic belt (Yin and Harrison, 2000). As stated by Zhang et al. (2013), the lower crust of the Gangdese magmatic arc underwent extensive granulite facies metamorphism during the Palaeocene and Eocene as recorded by deep-seated orthogneiss and paragneiss. These rocks are dominated by plagioclase, muscovite, biotite, and quartz with or without garnet and amphibole, as well as some sillimanite- and kyanite-bearing gneiss. The lower-crustal granulites of the Gangdese arc root underwent a long period of prograde metamorphism between the Eocene and the Miocene, primarily as a

result of the increasing pressures and temperatures generated by the thickening of the lower crust during continental collision. The higher-grade metamorphism took place in response to both higher temperatures and lower water activity, generating a succession of mineral assemblages that reflect progressive dehydration (Binns, 1964; Labotka et al., 1984; Guiraud et al., 2001; Weinberg and Hasalová, 2015). The water released during this metamorphic dehydration either filled grain boundaries and pore networks or may have entered surrounding blocks along fractures (Yardley, 1981; Bottrell et al., 1990; Yardley and Valley, 1997; Jackson et al., 2004).

It is here suggested that the thickening lower crust of the South Lhasa Terrane became dehydrated through metamorphic reactions of hydrous minerals during the India–Asia collision and intracontinental deformation. Examples of this include (i) muscovite dehydration involving a reaction proceeding at ~650–750 °C with the equilibrium equation of muscovite + plagioclase + quartz = K-feldspar + kyanite + H₂O (Thompson, 1983; Yardley and Valley, 1997); (ii) biotite dehydration at ~750–850 °C involves the equilibrium equation of biotite + sillimanite + quartz = K-feldspar + garnet/cordierite + H₂O (Phillips, 1981); (iii) and amphibole dehydration at ~850–900 °C involving the equilibrium equation of hornblende + plagioclase = clinopyroxene/garnet + H₂O (Wolf and Wyllie, 1994). The large quantity of water released by these long-term metamorphic dehydration reactions could have been stored at the crust–mantle boundary, an area that also preserved previously underplated basaltic melts. The continuous infiltration of additional water from these metamorphic dehydration reactions increased the water content of the basaltic melts; a process that eventually produced the fertile MMP and other Miocene mineralization-related magma that formed porphyry Cu deposits in Tibet.

6.4. New model of post-collisional porphyry Cu mineralization

The collision between India and Asia began at ~65–50 Ma, and the on-going collision and convergence of the plates resulted in the thickening and shortening of the continental crust and uplift of the Tibetan Plateau (Patriat and Achache, 1984; Klootwijk et al., 1992; Yin and Harrison, 2000; DeCelles et al., 2002; Mo et al., 2003; Ding et al., 2005; Chung et al., 2009). The Gangdese Batholith and the coeval Linzizong volcanics crop out throughout the South Lhasa Terrane (Wen, 2007; Mo et al., 2008; Ji et al., 2009). However, only two collision-related porphyry deposits have been discovered in this area to date. These are the ca. 45 Ma Jiru porphyry Cu deposit (Zheng et al., 2014b) and the ca. 52 Ma Sharang porphyry Mo deposit (Zhao et al., 2014). As discussed earlier, EG formed from magma generated by partial melting of a newly underplated basaltic region of the lower crust, which was originated from a mantle wedge that was metasomatized by Neo-Tethyan slab-derived fluids and oceanic sediments. The break-off of the subducted Neo-Tethyan slab during the early stages of the India–Asia collision may have caused asthenospheric upwelling and subsequent basaltic underplating (Fig. 14a; Lee et al., 2012). The basaltic melts inherited being highly oxidized arc magma characterized with high Cl, F, S, and Cu concentrations (Sillitoe, 1997; Li et al., 2011). The melts formed at the crust–mantle boundary and constitute the lower crust within the arc. However, when some of the melts ascended to the shallow surface together with the fractional crystallization of pyroxene, plagioclase, and magnetite in relatively dry conditions, the decompression and discharge of SO₂ through the contemporary Linzizong volcanism would have reduced their magmatic oxygen fugacity (Fig. 14a). This could account for the generation of magma forming the barren EG, as well as the fact that few porphyry deposits are associated with the Gangdese Batholith in Tibet. In particular, the Eocene formation of the Jiru porphyry Cu deposit may have been related to fragments of underthrusting ocean crust during continental collision, as shown by the

presence of mafic microgranular enclaves with high Sr/Y ratios (Niu et al., 2013; Sun et al., 2013b). The genesis of the Sharang porphyry Mo deposit was associated with the assimilation of old crustal material, as evidenced by the enriched Sr–Nd isotopic signatures of mineralization-related intrusions and the low Re contents of molybdenite from this deposit (Zhao et al., 2012, 2014).

Several models have been proposed to explain the geodynamic processes that formed the Miocene Gangdese porphyry Cu–Mo deposits and associated granites with high Sr/Y ratios (Chung et al., 2009; Hou et al., 2009; Ji et al., 2009; Li et al., 2011; Wu et al., 2014; Zheng et al., 2015). Most of these models explain the Miocene magmatism as a result of the convective removal of a thickened region of lithospheric mantle caused by gravitational instability and the subsequent upward counterflow of hotter asthenospheric mantle, although the timing of removal of this orogenic lithospheric mantle root has been assigned various ages of 30–15 Ma (Chung et al., 2009), 33–13 Ma (Ji et al., 2009), and 20–10 Ma (Li et al., 2011). Following Richards (2009) and Wu et al. (2014), it is here proposed that remelting of previously underplated basaltic magma during the Palaeocene and Eocene generated the fertile MMP and other magma associated with Miocene porphyry deposits. This model is supported by whole-rock Sr–Nd and zircon Hf isotopic compositions that are indistinguishable from those of the Palaeocene–Eocene Gangdese Batholith and the Linzizong volcanics (Figs. 8 and 9).

The model presented on Fig. 14b predicts a genetic link between earlier Neo-Tethyan subduction processes and the formation of porphyry Cu deposits in a post-collision tectonic setting. Long-lived subduction is likely responsible for the highly oxidized nature of fertile magma, a characteristic that is generated by the addition of oxidized components (as well as F, Cl, S, and Cu) to the sub-arc mantle. In addition, the long-term metamorphic dehydration associated with the India–Asia collision and subsequent crustal thickening and shortening was responsible for the high water contents of the magma, because the metamorphism released water that then replenished the basaltic melts at the base of the lower crust. In summary, metasomatism related to subducted oceanic crust, metamorphic dehydration of the thickened region of the lower crust, and the absence of coeval volcanism were all important controls on the genesis of fertile magma and the formation of the Miocene porphyry Cu deposits in Tibet.

7. Conclusions

The barren Eocene monzogranite (EG) and the fertile Miocene monzogranite porphyry (MMP) associated with the Dabu porphyry Cu–Mo deposit in southern Tibet have similar Sr–Nd–Hf isotopic compositions to the Palaeocene–Eocene Gangdese Batholith and the coeval Linzizong volcanics. All of these rocks formed from magma generated by partial melting or remelting of a basaltic source in the lower crust, which was underplated during the Palaeocene and Eocene. The basaltic melts were derived from a mantle wedge that was metasomatized by the Neo-Tethyan slab-derived fluids and oceanic sediments.

MMP formed under higher magmatic oxygen fugacity conditions and contained more water than EG did. The decompression and discharge of SO₂ during the coeval Linzizong volcanism might account for the low magmatic oxygen fugacity of EG and the limited development of porphyry Cu deposits associated with the Gangdese Batholith. The high water content of MMP probably reflects the continuous infiltration of additional water during metamorphic dehydration associated with the India–Asia collision and subsequent crust thickening and shortening.

The metasomatism related to subducted oceanic crust, the metamorphic dehydration of a thickened region of the lower crust, and an absence of coeval volcanism all contributed to the genesis of fertile

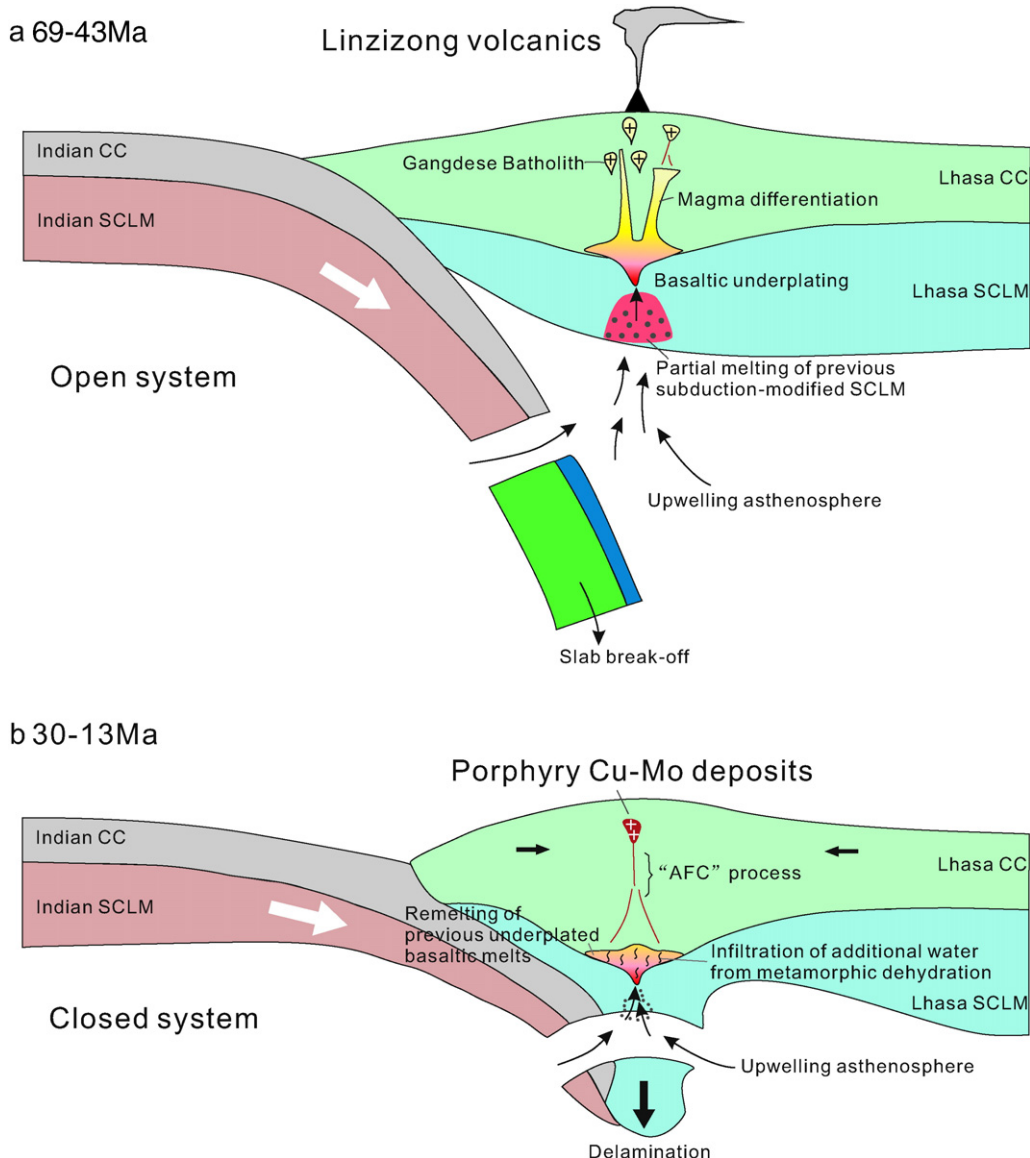


Fig. 14. Schematic model showing the tectonic evolution of GPCD from collisional to post-collisional stages and the genesis of barren and fertile magmas: (a) the subducted Neo-Tethyan slab rollback and subsequent break-off during the India–Asia collision resulted in the underplating of basaltic melts derived from a metasomatized mantle wedge during the long-lived subduction process at the crust–mantle boundary, which formed the Gangdese Batholith and Linzizong volcanics accompanied by the decompression and discharge of SO₂ in an open system; and (b) re-melting of previous underplated basaltic melts induced by the delamination of a thickened lithospheric mantle root, characterized by high magmatic oxygen fugacity inherited from the former arc-mantle and high water contents added by long-term metamorphic dehydration (leading to the generation of fertile porphyries for the post-collisional porphyry Cu–Mo deposits under compressional conditions in Tibet). Abbreviations: SCLM = subcontinental lithospheric mantle, CC = continental crust, LM = lithospheric mantle, OC = oceanic crust.

magma that is prospective for the formation of post-collision porphyry Cu–Mo deposits in Tibet.

Conflict of interest

We declare that we do not have any commercial or associative interest that represents a conflict of interest in connection with the work submitted.

Acknowledgments

We are grateful to Yongjun Lu and an anonymous reviewer, and Leon Bagas for their constructive comments and suggestions, which have largely improved this manuscript. This research was supported by the Commonweal Project from the Ministry of Land and Resources (201511015).

Appendix A. Supplementary data

Supplementary data to this article can be found online at <http://dx.doi.org/10.1016/j.oregeorev.2015.10.023>.

References

- Anser Li, Z.X., Aeolus Lee, C.T., 2004. The constancy of upper mantle fO₂ through time inferred from V/Sc ratios in basalts. *Earth Planet. Sci. Lett.* 228, 483–493.
- Asadi, S., Moore, F., Zaravandi, A., 2014. Discriminating productive and barren porphyry copper deposits in the southeastern part of the central Iranian volcano-plutonic belt, Kerman region, Iran: a review. *Earth Sci. Rev.* 138, 25–46.
- Ballard, J.R., Palin, M.J., Campbell, I.H., 2002. Relative oxidation states of magmas inferred from Ce(IV)/Ce(III) in zircon: application to porphyry copper deposits of northern Chile. *Contrib. Mineral. Petrol.* 144, 347–364.
- Ben Othman, D., White, W.M., Patchett, J., 1989. The geochemistry of marine sediments, island arc magma genesis, and crust–mantle recycling. *Earth Planet. Sci. Lett.* 94, 1–21.
- Binns, R., 1964. Zones of progressive regional metamorphism in the Willyama complex, Broken Hill district, New South Wales. *J. Geol. Soc. Aust.* 11, 283–330.

- Black, L.P., Kamo, S.L., Allen, C.M., Aleinikoff, J.N., Davis, D.W., Korsch, R.J., Foudoulis, C., 2003. TEMORA 1: a new zircon standard for Phanerozoic U-Pb geochronology. *Chem. Geol.* 200, 155–170.
- Blichert-Toft, J., Albarède, F., 1997. The Lu-Hf isotope geochemistry of chondrites and the evolution of the mantle–crust system. *Earth Planet. Sci. Lett.* 148, 243–258.
- Bottrell, S., Greenwood, P., Yardley, B., Shepherd, T., Spiro, B., 1990. Metamorphic and post-metamorphic fluid flow in the low-grade rocks of the Harlech Dome, north Wales. *J. Metamorph. Geol.* 8, 131–143.
- Brandon, A.D., Draper, D.S., 1996. Constraints on the origin of the oxidation state of mantle overlying subduction zones: an example from Simcoe, Washington, USA. *Geochim. Cosmochim. Acta* 60, 1739–1749.
- Buddington, A., Lindsley, D., 1964. Iron-titanium oxide minerals and synthetic equivalents. *J. Petrol.* 5, 310–357.
- Burnham, C.W., 1997. Magmas and hydrothermal fluids. In: Barnes, H.L. (Ed.), *Geochemistry of Hydrothermal Ore Deposits*, 3rd ed. John Wiley and Sons, New York, pp. 63–123.
- Canil, D., 1997. Vanadium partitioning and the oxidation state of Archaean komatiite magmas. *Nature* 389, 842–845.
- Carroll, M., Rutherford, M., 1985. Sulfide and sulfate saturation in hydrous silicate melts. *J. Geophys. Res. Solid Earth* 90 (C601–C612).
- Castillo, P.R., Janney, P.E., Solidum, R.U., 1999. Petrology and geochemistry of Camiguin Island, southern Philippines: insights to the source of adakites and other lavas in a complex arc setting. *Contrib. Mineral. Petrol.* 134, 33–51.
- Chen, L., Qin, K.Z., Li, G.M., Li, J.X., Xiao, B., Zhao, J.X., Fan, X., 2015. Zircon U-Pb ages, geochemistry, and Sr-Nd-Pb-Hf isotopes of the Nuri intrusive rocks in the Gangdese area, southern Tibet: constraints on timing, petrogenesis, and tectonic transformation. *Lithos* 212–215, 379–396.
- Chen, L., Qin, K.Z., Li, J.X., Xiao, B., Li, G.M., Zhao, J.X., Fan, X., 2012. Fluid inclusions and hydrogen, oxygen, sulfur isotopes of Nuri Cu-W-Mo deposit in the Southern Gangdese, Tibet. *Resour. Geol.* 62, 42–62.
- Chiaradia, M., 2013. Copper enrichment in arc magmas controlled by overriding plate thickness. *Nat. Geosci.* 7, 43–46.
- Chung, S.L., Chu, M.F., Ji, J., O'Reilly, S.Y., Pearson, N.J., Liu, D., Lee, T.Y., Lo, C.H., 2009. The nature and timing of crustal thickening in southern Tibet: geochemical and zircon Hf isotopic constraints from postcollisional adakites. *Tectonophysics* 477, 36–48.
- Cline, J.S., 1995. Genesis of porphyry copper deposits: the behavior of water, chloride, and copper in crystallizing melts. In: Pierce, F.W., Bolm, J.G. (Eds.), *Ariz. Geol. Soc. Dig.* 20, pp. 69–82.
- Cline, J.S., Bodnar, R.J., 1991. Can economic porphyry copper mineralization be generated by a typical calc-alkaline melt. *J. Geophys. Res.* 96, 8113–8126.
- Compston, W., Williams, I.S., Meyer, C., 1984. U-Pb geochronology of zircons from lunar breccia 73217 using a high massresolution ion microprobe. *J. Geophys. Res.* 89, B525–B534.
- Condie, K.C., 1989. Geochemical changes in basalts and andesites across the Archean-Proterozoic boundary: identification and significance. *Lithos* 23, 1–18.
- DeCelles, P.G., Robinson, D.M., Zandt, G., 2002. Implications of shortening in the Himalayan fold-thrust belt for uplift of the Tibetan Plateau. *Tectonics* 21 (12–1–12–25).
- Defant, M.J., Drummond, M.S., 1993. Mount St. Helens: potential example of the partial melting of the subducted lithosphere in a volcanic arc. *Geology* 21, 547–550.
- Deng, J., Wang, Q.F., Li, G.J., Santosh, M., 2014b. Cenozoic tectono-magmatic and metallogenetic processes in the Sanjiang region, southwestern China. *Earth Sci. Rev.* 138, 268–299.
- Deng, J., Wang, Q.F., Li, G.J., Li, C.S., Wang, C.M., 2014a. Tethys tectonic evolution and its bearing on the distribution of important mineral deposits in the Sanjiang region, SW China. *Gondwana Res.* 26, 419–437.
- Dilles, J.H., 2015. Zircon compositional evidence for sulfur-degassing from ore-forming arc magmas. *Econ. Geol.* 110, 241–251.
- Ding, L., Kapp, P., Wan, X., 2005. Paleocene-Eocene record of ophiolite obduction and initial India-Asia collision, South Central Tibet. *Tectonics* 24, TC3001.
- Ding, L., Kapp, P., Zhong, D., Deng, W., 2003. Cenozoic volcanism in Tibet: evidence for a transition from oceanic to continental subduction. *J. Petrol.* 44, 1833–1865.
- Dong, X., Zhang, Z., Santosh, M., 2010. Zircon U-Pb chronology of the Nyingtri group, southern Lhasa terrane, Tibetan Plateau: implications for Grenvillian and Pan-African provenance and Mesozoic-Cenozoic metamorphism. *J. Geol.* 118, 677–690.
- Du, D., Yang, Z., Li, Q., Liu, Y., Ge, S., Wang, H., 2012. Determination of Eocene porphyritic monzogranite intrusions in Tinggong ore district of Tibet and its geological significance. *Mineral Deposits* 31, 745–757 (in Chinese with English abstract).
- Eichelberger, J., 1995. Silicic volcanism: ascent of viscous magmas from crustal reservoirs. *Annu. Rev. Earth Planet. Sci.* 23, 41–64.
- Elburg, M.A., van Bergen, M., Hoogewerff, J., Foden, J., Vroon, P., Zulkarnain, I., Nasution, A., 2002. Geochemical trends across an arc-continent collision zone: magma sources and slab-wedge transfer processes below the Pantar Strait volcanoes, Indonesia. *Geochim. Cosmochim. Acta* 66, 2771–2789.
- Elhlou, S., Belousova, E., Griffin, W.L., Pearson, N.J., O'Reilly, S.Y., 2006. Trace element and isotopic composition of GJ-red zircon standard by laser ablation. *Geochim. Cosmochim. Acta* 70, A158.
- Feig, S., Koepke, J., Snow, J., 2006. Effect of water on tholeiitic basalt phase equilibria: an experimental study under oxidizing conditions. *Contrib. Mineral. Petrol.* 152, 611–638.
- Ferry, J.M., Watson, E.B., 2007. New thermodynamic models and revised calibrations for the Ti-in-zircon and Zr-in-rutile thermometers. *Contrib. Mineral. Petrol.* 154, 429–437.
- Foster, M.D., 1960. Interpretation of composition of trioctahedral micas. *US Geol. Surv. Prof. Pap.* 354B, 1–49.
- Frost, D.J., McCammon, C.A., 2008. The redox state of earth's mantle. *Annu. Rev. Earth Planet. Sci.* 36, 389–420.
- Gao, Y.F., Hou, Z.Q., Kamber, B.S., Wei, R.H., Meng, X.J., Zhao, R.S., 2007. Lamproitic rocks from a continental collision zone: evidence for recycling of subducted tethyan oceanic sediments in the mantle beneath southern Tibet. *J. Petrol.* 48, 729–752.
- Gao, J., Klemd, R., Long, L., Xiong, X., Qian, Q., 2009. Adakitic signature formed by fractional crystallization: an interpretation for the Neo-Proterozoic meta-plagiogranites of the NE Jiangxi ophiolitic mélange belt, South China. *Lithos* 110, 277–293.
- Gao, S., Liu, X., Yuan, H., Hattendorf, B., Günther, D., Chen, L., Hu, S., 2002. Determination of forty two major and trace elements in USGS and NIST SRM glasses by laser ablation-inductively coupled plasma-mass spectrometry. *Geostand. Newslett.* 26, 181–196.
- Gao, Y.F., Yang, Z.S., Santosh, M., Hou, Z.Q., Wei, R.H., Tian, S.H., 2010. Adakitic rocks from slab melt-modified mantle sources in the continental collision zone of southern Tibet. *Lithos* 119, 651–663.
- Griffin, W.L., Pearson, N.J., Belousova, E.A., Saeed, A., 2006. Comment: Hf-isotope heterogeneity in zircon 91500. *Chem. Geol.* 233, 358–363.
- Griffin, W.L., Wang, X., Jackson, S.E., Pearson, N.J., O'Reilly, S.Y., Xu, X.S., Zhou, X.M., 2002. Zircon chemistry and magma mixing, SE China: in-situ analysis of Hf isotopes, Tonglu and Pingtan igneous complexes. *Lithos* 61, 237–269.
- Guan, Q., Zhu, D.C., Zhao, Z.D., Dong, G.C., Zhang, L.L., Li, X.W., Liu, M., Mo, X.X., Liu, Y.S., Yuan, H.L., 2012. Crustal thickening prior to 38 Ma in southern Tibet: evidence from lower crust-derived adakitic magmatism in the Gangdese Batholith. *Gondwana Res.* 21, 88–99.
- Guiraud, M., Powell, R., Rebay, G., 2001. H₂O in metamorphism and unexpected behaviour in the preservation of metamorphic mineral assemblages. *J. Metamorph. Geol.* 19, 445–454.
- Guo, Z., Wilson, M., Zhang, M., Cheng, Z., Zhang, L., 2013. Post-collisional, K-rich mafic magmatism in south Tibet: constraints on Indian slab-to-wedge transport processes and plateau uplift. *Contrib. Mineral. Petrol.* 165, 1311–1340.
- Haschke, M., Ahmadian, J., Murata, M., McDonald, I., 2010. Copper mineralization prevented by arc-root delamination during Alpine-Himalayan collision in central Iran. *Econ. Geol.* 105, 855–865.
- Henry, D.J., 2005. The Ti-saturation surface for low-to-medium pressure metapelitic biotites: implications for geothermometry and Ti-substitution mechanisms. *Am. Mineral.* 90, 316–328.
- Hildreth, W., Moorbath, S., 1988. Crustal contributions to arc magmatism in the Andes of central Chile. *Contrib. Mineral. Petrol.* 98, 455–489.
- Hoskin, P., Black, L., 2000. Metamorphic zircon formation by solid-state recrystallization of protolith igneous zircon. *J. Metamorph. Geol.* 18, 423–439.
- Hoskin, P.W., Schaltegger, U., 2003. The composition of zircon and igneous and metamorphic petrogenesis. *Rev. Mineral. Geochem.* 53, 27–62.
- Hou, Z.Q., Duan, L.F., Lu, Y.J., Zheng, Y.C., Zhu, D.C., Yang, Z.M., Yang, Z.S., Wang, B.D., Pei, Y.R., Zhao, Z.D., McCraig, T.C., 2015a. Lithospheric architecture of the Lhasa Terrane and its control on ore deposits in the Himalayan-Tibetan orogen. *Econ. Geol.* 110, 1541–1575.
- Hou, Z.Q., Yang, Z.M., Lu, Y.J., Kemp, A., Zheng, Y.C., Li, Q.Y., Tang, J.X., Yang, Z.S., Duan, L.F., 2015b. A genetic linkage between subduction-and collision-related porphyry Cu deposits in continental collision zones. *Geology* 43, 247–250.
- Hou, Z.Q., Yang, Z.M., Qu, X.M., Meng, X.J., Li, Z.Q., Beaudoin, G., Rui, Z.Y., Gao, Y.F., Zaw, K., 2009. The Miocene Gangdese porphyry copper belt generated during post-collisional extension in the Tibetan orogen. *Ore Geol. Rev.* 36, 25–51.
- Hou, Z.Q., Zhang, H.R., Pan, X.F., Yang, Z.M., 2011. Porphyry Cu (–Mo-Au) deposits related to melting of thickened mafic lower crust: examples from the eastern Tethyan metallogenic domain. *Ore Geol. Rev.* 39, 21–45.
- Hu, Z.C., Liu, Y.S., Gao, S., Liu, W.G., Zhang, W., Tong, X.R., Lin, L., Zong, K.Q., Li, M., Chen, H.H., 2012. Improved in situ Hf isotope ratio analysis of zircon using newly designed X Skinner cone and jet sample cone in combination with the addition of nitrogen by laser ablation multiple collector ICP-MS. *J. Anal. At. Spectrom.* 27, 1391–1399.
- Hu, Y.B., Liu, J.Q., Ling, M.X., Ding, W., Liu, Y., Zartman, R.E., Ma, X.F., Liu, D.Y., Zhang, C.C., Sun, S.J., Zhang, L.P., Wu, K., Sun, W.D., 2015. The formation of Qulong adakites and their relationship with porphyry copper deposit: geochemical constraints. *Lithos* 220–223, 60–80.
- Jackson, J.A., Austrheim, H., McKenzie, D., Priestley, K., 2004. Metastability, mechanical strength, and the support of mountain belts. *Geology* 32, 625.
- Jamali, H., Mehrabi, B., 2015. Relationships between arc maturity and Cu-Mo-Au porphyry and related epithermal mineralization at the Cenozoic Arasbaran magmatic belt. *Ore Geol. Rev.* 65, 487–501.
- Ji, W.Q., Wu, F.Y., Chung, S.L., Li, J.X., Liu, C.Z., 2009. Zircon U-Pb geochronology and Hf isotopic constraints on petrogenesis of the Gangdese batholith, southern Tibet. *Chem. Geol.* 262, 229–245.
- Ji, W.Q., Wu, F.Y., Liu, C.Z., Chung, S.L., 2012. Early Eocene crustal thickening in southern Tibet: new age and geochemical constraints from the Gangdese batholith. *J. Asian Earth Sci.* 53, 82–95.
- Kay, S.M., Mpodozis, C., 2001. Central Andean ore deposits linked to evolving shallow subduction systems and thickening crust. *GSA Today* 11, 4–9.
- Kelley, K.A., Cottrell, E., 2009. Water and the oxidation state of subduction zone magmas. *Science* 325, 605–607.
- Kelley, K.A., Cottrell, E., 2012. The influence of magmatic differentiation on the oxidation state of Fe in a basaltic arc magma. *Earth Planet. Sci. Lett.* 329–330, 109–121.
- Kind, R., Ni, J., Zhao, W., Wu, J., Yuan, X., Zhao, L., Sandvol, E., Reese, C., Nabelek, J., Hearn, T., 1996. Evidence from earthquake data for a partially molten crustal layer in southern Tibet. *Science* 274, 1692–1694.
- Klootwijk, C.T., Gee, J.S., Pearce, J.W., Smith, G.M., McFadden, P.L., 1992. An early India-Asia contact: paleomagnetic constraints from Ninetyeast ridge, ODP Leg 121. *Geology* 20, 395–398.
- La Tourette, T., Burnett, D., Bacon, C.R., 1991. Uranium and minor-element partitioning in Fe-Ti oxides and zircon from partially melted granodiorite, Crater Lake, Oregon. *Geochim. Cosmochim. Acta* 55, 457–469.

- Labotka, T.C., White, C.E., Papike, J., 1984. The evolution of water in the contact-metamorphic aureole of the Duluth Complex, northeastern Minnesota. *Geol. Soc. Am. Bull.* 95, 788–804.
- Lang, X.H., Tang, J.X., Li, Z.J., Huang, Y., Ding, F., Yang, H.H., Xie, F.W., Zhang, L., Wang, Q., Zhou, Y., 2014. U-Pb and Re-Os geochronological evidence for the Jurassic porphyry metallogenic event of the Xiongcuo district in the Gangdese porphyry copper belt, southern Tibet, PRC. *J. Asian Earth Sci.* 79, 608–622.
- Lange, R.A., Frey, H.M., Hector, J., 2009. A thermodynamic model for the plagioclase-liquid hygrometer/thermometer. *Am. Mineral.* 94, 494–506.
- Lattard, D., Sauerzapf, U., Käsemann, M., 2005. New calibration data for the Fe-Ti oxide thermo-oxybarometers from experiments in the Fe-Ti-O system at 1 bar, 1,000–1,300 °C and a large range of oxygen fugacities. *Contrib. Mineral. Petrol.* 149, 735–754.
- Lécuyer, C., Ricard, Y., 1999. Long-term fluxes and budget of ferric iron: implication for the redox states of the earth's mantle and atmosphere. *Earth Planet. Sci. Lett.* 165, 197–211.
- Lee, C.T., 2013. Economic geology: copper conundrums. *Nat. Geosci.* 7, 10–11.
- Lee, H.Y., Chung, S.L., Ji, J., Qian, Q., Gallet, S., Lo, C.H., Lee, T.Y., Zhang, Q., 2012. Geochemical and Sr-Nd isotopic constraints on the genesis of the Cenozoic Linzizong volcanic successions, southern Tibet. *J. Asian Earth Sci.* 53, 96–114.
- Lee, H.Y., Chung, S.L., Lo, C.H., Ji, J., Lee, T.Y., Qian, Q., Zhang, Q., 2009. Eocene Neotethyan slab breakup in southern Tibet inferred from the Linzizong volcanic record. *Tectonophysics* 477, 20–35.
- Lee, H., Chung, S., Wang, Y., Zhu, D., Yang, J., Song, B., Liu, D., Wu, F., 2007. Age, petrogenesis and geological significance of the Linzizong volcanic successions in the Linzhou basin, southern Tibet: evidence from zircon U-Pb dates and Hf isotopes. *Acta Petrol. Sin.* 23, 493–500 (in Chinese with English abstract).
- Lee, C.T., Luffi, P., Le Roux, V., Dasgupta, R., Albarede, F., Leeman, W.P., 2010. The redox state of arc mantle using Zn/Fe systems. *Nature* 468, 681–685.
- Leng, C.B., Zhang, X.C., Zhong, H., Hu, R.Z., Zhou, W.D., Li, C., 2013. Re-Os molybdenite ages and zircon Hf isotopes of the Gangjiang porphyry Cu-Mo deposit in the Tibetan Orogen. *Mineral. Deposita* 48, 585–602.
- Lepage, L.D., 2003. ILMAT: an excel worksheet for ilmenite–magnetite geothermometry and geobarometry. *Comput. Geosci.* 29, 673–678.
- Li, J.X., Qin, K.Z., Li, G.M., Xiao, B., Chen, L., Zhao, J.X., 2011. Post-collisional ore-bearing adakitic porphyries from Gangdese porphyry copper belt, southern Tibet: melting of thickened juvenile arc lower crust. *Lithos* 126, 265–277.
- Liang, Q., Grégoire, D.C., 2000. Determination of trace elements in twenty six Chinese geochemistry reference materials by inductively coupled plasma-mass spectrometry. *Geostand. Newslett.* 24, 51–63.
- Ling, W.L., Duan, R.C., Xie, X.J., Zhang, Y.Q., Zhang, J.B., Cheng, J.P., Liu, X.M., Yang, H.M., 2009. Contrasting geochemistry of the Cretaceous volcanic suites in Shandong province and its implications for the Mesozoic lower crust delamination in the eastern North China craton. *Lithos* 113, 640–658.
- Liu, Y., Hou, Z.Q., Tian, S.H., Zhang, Q.C., Zhu, Z.M., Liu, J.H., 2015a. Zircon U-Pb ages of the Mianning–Dechang syenites, Sichuan Province, southwestern China: constraints on the giant REE mineralization belt and its regional geological setting. *Ore Geol. Rev.* 64, 554–568.
- Liu, Y., Zhang, R.Q., Zhang, Z.Y., Shi, G.H., Zhang, Q.C., Abuduwayiti, M., Liu, J.H., 2015b. Mineral inclusions and SHRIMP U-Pb dating of zircons from the Alamas nephrite and granodiorite: implications for the genesis of a magnesian skarn deposit. *Lithos* 212–215, 128–144.
- Liu, Y., Chen, Z.Y., Yang, Z.S., Sun, X., Zhu, Z.M., Zhang, Q.C., 2015c. Mineralogical and geochemical studies of brecciated ores in the Dalucuo REE deposit, Sichuan Province, southwestern China. *Ore Geol. Rev.* 70, 613–636.
- Liu, Y., Deng, J., Shi, G.H., Sun, X., Yang, L.Q., 2012. Genesis of the Xuebaoding W-Sn-Be crystal deposits in southwest China: evidence from fluid inclusions, stable isotopes and ore elements. *Resour. Geol.* 62, 159–173.
- Liu, D., Zhao, Z.D., Zhu, D.C., Niu, Y.L., DePaolo, D.J., Mark Harrison, T., Mo, X.X., Dong, G.C., Zhou, S., Sun, C.G., Zhang, Z.C., Liu, J.L., 2014. Postcollisional potassic and ultrapotassic rocks in southern Tibet: mantle and crustal origins in response to India–Asia collision and convergence. *Geochim. Cosmochim. Acta* 143, 207–231.
- Liu, D., Zhao, Z.D., Zhu, D.C., Niu, Y.L., Harrison, T.M., 2013. Zircon xenocrysts in Tibetan ultrapotassic magmas: imaging the deep crust through time. *Geology* 42, 43–46.
- Liu, Y., Zhu, Z.M., Chen, C., Zhang, S.P., Sun, X., Yang, Z.S., Liang, W., 2015d. Geochemical and mineralogical characteristics of weathered ore in the Dalucuo REE deposit, Mianning–Dechang REE Belt, western Sichuan Province, southwestern China. *Ore Geol. Rev.* 71, 437–456.
- Loucks, R.R., 2014. Distinctive composition of copper-ore-forming arcmagmas. *Aust. J. Earth Sci.* 61, 5–16.
- Lu, Y.J., Kerrich, R., Cawood, P.A., McCuaig, T.C., Hart, C.J.R., Li, Z.X., Hou, Z.Q., Bagas, L., 2012. Zircon SHRIMP U-Pb geochronology of potassic felsic intrusions in western Yunnan, SW China: constraints on the relationship of magmatism to the Jinsha suture. *Gondwana Res.* 22, 737–747.
- Lu, Y.J., Kerrich, R., Kemp, A.I., McCuaig, T.C., Hou, Z.Q., Hart, C.J., Li, Z.X., Cawood, P.A., Bagas, L., Yang, Z.M., 2013. Intracontinental Eocene-Oligocene porphyry Cu mineral systems of Yunnan, western Yangtze craton, China: compositional characteristics, sources, and implications for continental collision metallogenesis. *Econ. Geol.* 108, 1541–1576.
- Lu, Y.J., Loucks, R.R., Fiorentini, M.L., Yang, Z.M., Hou, Z.Q., 2015. Fluid flux melting generated post-collisional high-Sr/Y copper-ore-forming water-rich magmas in Tibet. *Geology* 43, 583–586.
- Ludwig, K.R., 2003. User's Manual for Isoplot 3, a Geochronological Toolkit for Microsoft Excel. Berkeley Geochronology Center Special Publication 4.
- Ludwig, K.R., 2009. Squid 2: A User Manual. Berkeley Geochronology Center Special Publication 4.
- Ma, L., Wang, B.D., Jiang, Z.Q., Wang, Q., Li, Z.X., Wyman, D.A., Zhao, S.R., Yang, J.H., Gou, G.N., Guo, H.F., 2014. Petrogenesis of the Early Eocene adakitic rocks in the Napuri area, southern Lhasa: partial melting of thickened lower crust during slab break-off and implications for crustal thickening in southern Tibet. *Lithos* 196–197, 321–338.
- Ma, L., Wang, Q., Wyman, D.A., Jiang, Z.Q., Yang, J.H., Li, Q.L., Gou, G.N., Guo, H.F., 2013. Late Cretaceous crustal growth in the Gangdese area, southern Tibet: petrological and Sr-Nd-Hf-O isotopic evidence from Zhengga diorite-gabbro. *Chem. Geol.* 349–350, 54–70.
- Mao, J.W., Pirajno, F., Lehmann, B., Luo, M.C., Berzina, A., 2014. Distribution of porphyry deposits in the Eurasian continent and their corresponding tectonic settings. *J. Asian Earth Sci.* 79, 576–584.
- Martin, H., Smithies, R.H., Rapp, R., Moyen, J.F., Champion, D., 2005. An overview of adakite, tonalite-trondhjemite-granodiorite (TTG), and sanukitoid: relationships and some implications for crustal evolution. *Lithos* 79, 1–24.
- McKay, G., Le, L., Wagstaff, J., Crozaz, G., 1994. Experimental partitioning of rare earth elements and strontium: constraints on petrogenesis and redox conditions during crystallization of Antarctic angrite Lewis Cliff 86010. *Geochim. Cosmochim. Acta* 58, 2911–2919.
- Meng, X.J., 2004. The Metallogeny of the Mioeene Gangdese Porphyry Copper Belt in Tibetan Collisional Orogen (Ph.D. thesis) Chinese Academy of Geological Sciences, Beijing (105 pp., in Chinese with English abstract).
- Middlemost, E.A.K., 1994. Naming materials in the magma/igneous rock system. *Earth Sci. Rev.* 37, 215–224.
- Miller, C., Schuster, R., Klötzli, U., Frank, W., Purtscheller, F., 1999. Post-collisional potassic and ultrapotassic magmatism in SW Tibet: geochemical and Sr-Nd-Pb-O isotopic constraints for mantle source characteristics and petrogenesis. *J. Petrol.* 40, 1399–1424.
- Mo, X.X., Hou, Z.Q., Niu, Y.L., Dong, G.C., Qu, X.M., Zhao, Z.D., Yang, Z.M., 2007. Mantle contributions to crustal thickening during continental collision: evidence from Cenozoic igneous rocks in southern Tibet. *Lithos* 96, 225–242.
- Mo, X.X., Niu, Y.L., Dong, G.C., Zhao, Z.D., Hou, Z.Q., Zhou, S., Ke, S., 2008. Contribution of syncollisional felsic magmatism to continental crust growth: a case study of the Paleogene Linzizong volcano succession in southern Tibet. *Chem. Geol.* 250, 49–67.
- Mo, X.X., Zhao, Z.D., Deng, J.F., Dong, G.C., Zhou, S., Guo, T.Y., Zhang, S.Q., Wang, L.L., 2003. Response of volcanism to the India-Asia collision. *Earth Sci. Front.* 10, 135–148 (in Chinese with English abstract).
- Moyen, J.F., 2009. High Sr/Y and La/Yb ratios: the meaning of the "adakitic signature". *Lithos* 112, 556–574.
- Mullen, E.K., McCallum, I.S., 2013. Coexisting pseudobrookite, ilmenite, and titanomagnetite in hornblende andesite of the Coleman Pinnacle flow, Mount Baker, Washington: evidence for a highly oxidized arc magma. *Am. Mineral.* 98, 417–425.
- Niu, Y.L., Zhao, Z.D., Zhu, D.C., Mo, X.X., 2013. Continental collision zones are primary sites for net continental crust growth – a testable hypothesis. *Earth Sci. Rev.* 127, 96–110.
- O'Neill, H.S., 1987. Quartz-fayalite-iron and quartz-fayalite-magnetite equilibria and the free energy of formation of fayalite (Fe_2SiO_4) and magnetite (Fe_3O_4). *Am. Mineral.* 72, 67–75.
- Oyarzun, R., Márquez, A., Lillo, J., López, I., Rivera, S., 2001. Giant versus small porphyry copper deposits of Cenozoic age in northern Chile: adakitic versus normal calc-alkaline magmatism. *Mineral. Deposita* 36, 794–798.
- Pan, G.T., Mo, X.X., Hou, Z.Q., Zhu, D.C., Wang, L.Q., Li, G.M., Zhao, Z.D., Geng, Q.R., Liao, Z.L., 2006. Spatial-temporal framework of the Gangdese Orogenic Belt and its evolution. *Acta Petrol. Sin.* 22, 521–533 (in Chinese with English abstract).
- Parkinson, I.J., Arculus, R.J., 1999. The redox state of subduction zones: insights from arc-peridotites. *Chem. Geol.* 160, 409–423.
- Patriat, P., Achache, J., 1984. India-Eurasia collision chronology has implications for crustal shortening and driving mechanism of plates. *Nature* 311, 615–621.
- Pearce, J.A., Parkinson, I.J., 1993. Trace element models for mantle melting: application to volcanic arc petrogenesis. *Geol. Soc. Spec. Publ.* 76, 373–403.
- Pearce, N.J., Perkins, W.T., Westgate, J.A., Gorton, M.P., Jackson, S.E., Neal, C.R., Chereny, S.P., 1997. A compilation of new and published major and trace element data for NIST SRM 610 and NIST SRM 612 glass reference materials. *Geostand. Newslett.* 21, 115–144.
- Peccerillo, A., Taylor, S.R., 1976. Geochemistry of Eocene calc-alkaline volcanic rocks from the Kastamonu area, Northern Turkey. *Contrib. Mineral. Petrol.* 58, 63–81.
- Phillips, G.N., 1981. Water activity changes across an amphibolite–granulite facies transition, Broken Hill, Australia. *Contrib. Mineral. Petrol.* 75, 377–386.
- Plank, T., Langmuir, C.H., 1998. The chemical composition of subducting sediment and its consequences for the crust and mantle. *Chem. Geol.* 145, 325–394.
- Pokrovski, G.S., Borisova, A.Y., Harrichoury, J.C., 2008. The effect of sulfur on vapor–liquid fractionation of metals in hydrothermal systems. *Earth Planet. Sci. Lett.* 266, 345–362.
- Qu, X.M., Hou, Z.Q., Guo, L.J., Xu, W.C., 2004. Source compositions and crustal contaminations of adakitic ore-bearing porphyries in the Gangdese copper belt: Nd, Sr, Pb and O isotope constraints. *Acta Geol. Sin.* 78, 813 (in Chinese with English abstract).
- Qu, X.M., Hou, Z.Q., Khin, Z., Li, Y.G., 2007. Characteristics and genesis of Gangdese porphyry copper deposits in the southern Tibetan Plateau: preliminary geochemical and geochronological results. *Ore Geol. Rev.* 31, 205–223.
- Richards, J.P., 2003. Tectono-magmatic precursors for porphyry Cu-(Mo-Au) deposit formation. *Econ. Geol.* 98, 1515–1533.
- Richards, J.P., 2009. Postsubduction porphyry Cu-Au and epithermal Au deposits: products of remelting of subduction-modified lithosphere. *Geology* 37, 247–250.
- Richards, J.P., 2011a. High Sr/Y arc magmas and porphyry Cu ± Mo ± Au deposits: just add water. *Econ. Geol.* 106, 1075–1081.
- Richards, J.P., 2011b. Magmatic to hydrothermal metal fluxes in convergent and collided margins. *Ore Geol. Rev.* 40, 1–26.
- Richards, J.P., 2014. Tectonic, magmatic, and metallogenetic evolution of the Tethyan orogen: from subduction to collision. *Ore Geol. Rev.* 70, 323–345.

- Richards, J.P., 2015. The oxidation state, and sulfur and Cu contents of arc magmas: implications for metallogeny. *Lithos* 233, 27–45.
- Richards, J.P., Spell, T., Rameh, E., Razique, A., Fletcher, T., 2012. High Sr/Y magmas reflect arc maturity, high magmatic water content, and porphyry Cu ± Mo ± Au potential: examples from the Tethyan arcs of Central and Eastern Iran and Western Pakistan. *Econ. Geol.* 107, 295–332.
- Ridolfi, F., Renzulli, A., Puerini, M., 2009. Stability and chemical equilibrium of amphibole in calc-alkaline magmas: an overview, new thermobarometric formulations and application to subduction-related volcanoes. *Contrib. Mineral. Petrol.* 160, 45–66.
- Rowe, M.C., Kent, A.J.R., Nielsen, R.L., 2009. Subduction influence on oxygen fugacity and trace and volatile elements in basalts across the Cascade volcanic arc. *J. Petrol.* 50, 61–91.
- Sauerzapf, U., Lattard, D., Burchard, M., Engelmann, R., 2008. The titanomagnetite-ilmenite equilibrium: new experimental data and thermo-oxybarometric application to the crystallization of basic to intermediate rocks. *J. Petrol.* 49, 1161–1185.
- Seedorff, E., Dilles, J., Proffett, J., Einaudi, M., Zurcher, L., Stavast, W., Johnson, D., Barton, M., 2005. Porphyry Deposits: Characteristics and Origin of Hypogene Features. *Economic Geology* 100th Anniversary vol. 29 pp. 251–298.
- Shabani, A., 2010. An investigation on the composition of biotite from Mashhad granitoids, NE Iran. *J. Sci. Islam. Repub. Iran* 21.
- Shafiei, B., Haschke, M., Shahabpour, J., 2009. Recycling of orogenic arc crust triggers porphyry Cu mineralization in Kerman Cenozoic arc rocks, southeastern Iran. *Mineral. Deposita* 44, 265–283.
- Shen, P., Pan, H., 2013. Country-rock contamination of magmas associated with the Baogutu porphyry Cu deposit, Xinjiang, China. *Lithos* 177, 451–469.
- Sillitoe, R., 1997. Characteristics and controls of the largest porphyry copper-gold and epithermal gold deposits in the circum-Pacific region. *Aust. J. Earth Sci.* 44, 373–388.
- Sillitoe, R.H., 2010. Porphyry copper systems. *Econ. Geol.* 105, 3–41.
- Sisson, T., 1994. Hornblende-melt trace-element partitioning measured by ion microprobe. *Chem. Geol.* 117, 331–344.
- Stern, R., 2001. A new isotopic and trace-element standard for the ion-microprobe: preliminary thermal ionisation mass spectrometry (TIMS) U-Pb and electron micro-probe data. *Geological Survey of Canada Current Research* 2001–F1 (11 pp.).
- Sun, S.S., McDonough, W., 1989. Chemical and isotopic systematics of oceanic basalts: implications for mantle composition and processes. *Geol. Soc. Lond. Spec. Publ.* 42, 313–345.
- Sun, X., Zheng, Y.Y., Wu, S., Li, M., Ouyang, H.T., Geng, R.R., 2013b. Mafic enclaves at Jiru porphyry Cu deposit, southern Tibet: implication for the Eocene magmatic-hydrothermal Cu mineralization. *Acta Geol. Sin. (Engl. Ed.)* 87, 778–782.
- Sun, X., Zheng, Y.Y., Wu, S., You, Z.M., Wu, X., Li, M., Zhou, T.C., Dong, J., 2013c. Mineralization age and petrogenesis of associated intrusions in the Mingze-Chengba porphyry-skarn Mo-Cu deposit, Gangdese. *Acta Petrol. Sin.* 29, 1392–1406 (in Chinese with English abstract).
- Sun, W.D., Arculus, R.J., Kamenetsky, V.S., Binns, R.A., 2004. Release of gold-bearing fluids in convergent margin magmas prompted by magnetite crystallization. *Nature* 431, 975–978.
- Sun, W.D., Huang, R.F., Li, H., Hu, Y.B., Zhang, C.C., Sun, S.J., Zhang, L.P., Ding, X., Li, C.Y., Zartman, R.E., Ling, M.X., 2015. Porphyry deposits and oxidized magmas. *Ore Geol. Rev.* 65, 97–131.
- Sun, W.D., Liang, H.Y., Ling, M.X., Zhan, M.Z., Ding, X., Zhang, H., Yang, X.Y., Li, Y.L., Ireland, T.R., Wei, Q.R., Fan, W.M., 2013a. The link between reduced porphyry copper deposits and oxidized magmas. *Geochim. Cosmochim. Acta* 103, 263–275.
- Tatsumi, Y., Hamilton, D., Nesbitt, R., 1986. Chemical characteristics of fluid phase released from a subducted lithosphere and origin of arc magmas: evidence from high-pressure experiments and natural rocks. *J. Volcanol. Geotherm. Res.* 29, 293–309.
- Thompson, A., 1983. Fluid-absent metamorphism. *J. Geol. Soc.* 140, 533–547.
- Uchida, E., Endo, S., Makino, M., 2007. Relationship between solidification depth of granitic rocks and formation of hydrothermal ore deposits. *Resour. Geol.* 57, 47–56.
- Walker, J.A., Roggensack, K., Patino, L.C., Cameron, B.I., Matfias, O., 2003. The water and trace element contents of melt inclusions across an active subduction zone. *Contrib. Mineral. Petrol.* 146, 62–77.
- Wang, R., Richards, J.P., Hou, Z.Q., Yang, Z.M., 2014d. Extent of underthrusting of the Indian plate beneath Tibet controlled the distribution of Miocene porphyry Cu-Mo ± Au deposits. *Mineral. Deposita* 49, 165–173.
- Wang, R., Richards, J.P., Hou, Z.Q., Yang, Z.M., DuFrane, S.A., 2014c. Increased magmatic water content—the key to oligo-miocene porphyry Cu-Mo ± Au formation in the Eastern Gangdese Belt, Tibet. *Econ. Geol.* 109, 1315–1339.
- Wang, R., Richards, J.P., Hou, Z.Q., Yang, Z.M., Gou, Z.B., DuFrane, S.A., 2014b. Increasing magmatic oxidation state from Paleocene to Miocene in the Eastern Gangdese Belt, Tibet: implication for collision-related porphyry Cu-Mo ± Au mineralization. *Econ. Geol.* 109, 1943–1965.
- Wang, B.D., Chen, J.L., Xu, J.F., Wang, L.Q., 2014a. Geochemical and Sr-Nd-Pb-Os isotopic compositions of Miocene ultrapotassic rocks in southern Tibet: petrogenesis and implications for the regional tectonic history. *Lithos* 208–209, 237–250.
- Wang, LL., Mo, X.X., Li, B., Dong, G.C., Zhao, Z.D., 2006. Geochronology and geochemistry of the ore-bearing porphyry in Qulong Cu (Mo) ore deposit, Tibet. *Acta Petrol. Sin.* 22, 1001–1008 (in Chinese with English abstract).
- Watson, E.B., Harrison, T.M., 1983. Zircon saturation revisited: temperature and composition effects in a variety of crustal magma types. *Earth Planet. Sci. Lett.* 64, 295–304.
- Weinberg, R.F., Hasalová, P., 2015. Water-fluxed melting of the continental crust: a review. *Lithos* 212, 158–188.
- Wen, D.R., 2007. The Gangdese Batholith, Southern Tibet: Ages, Geochemical Characteristics and Petrogenesis (Ph.D. thesis) National Taiwan University (140 pp.).
- Wen, D.R., Chung, S.L., Song, B., Iizuka, Y., Yang, H.J., Ji, J., Liu, D., Gallet, S., 2008. Late Cretaceous Gangdese intrusions of adakitic geochemical characteristics, SE Tibet: petrogenesis and tectonic implications. *Lithos* 105, 1–11.
- Williams, I.S., 1998. U-Th-Pb geochronology by ion microprobe. *Rev. Econ. Geol.* 7, 1–35.
- Wolf, M.B., Wyllie, P.J., 1994. Dehydration-melting of amphibolite at 10 kbar: the effects of temperature and time. *Contrib. Mineral. Petrol.* 115, 369–383.
- Wones, D., Eugster, H., 1965. Stability of biotite-experiment theory and application. *Am. Mineral.* 50, 1228–1272.
- Wood, B.J., Bryndzia, L.T., Johnson, K.E., 1990. Mantle oxidation state and its relationship to tectonic environment and fluid speciation. *Science* 248, 337–345.
- Wu, C., Yang, J., Robinson, P.T., Wooden, J.L., Mazdab, F.K., Gao, Y., Wu, S., Chen, Q., 2009. Geochemistry, age and tectonic significance of granitic rocks in north Altun, northwest China. *Lithos* 113, 423–436.
- Wu, S., Zheng, Y.Y., Sun, X., Liu, S.A., Geng, R.R., You, Z.M., Ouyang, H.T., Lei, D., Zhao, Z.Y., 2014. Origin of the Miocene porphyries and their mafic microgranular enclaves from Dabu porphyry Cu-Mo deposit, southern Tibet: implications for magma mixing/mining and mineralization. *Int. Geol. Rev.* 56, 571–595.
- Yang, Z.M., 2008. The Qulong Giant Porphyry Copper Deposit in Tibet: Magmatism and Mineralization (Ph. D. thesis) Institute of Geology Chinese Academy of Geological Sciences, Beijing (144 pp., in Chinese with English abstract).
- Yang, Z.M., Lu, Y.J., Hou, Z.Q., Chang, Z.S., 2015. High-Mg diorite from qulong in southern Tibet: implications for the genesis of adakite-like intrusions and associated porphyry Cu deposits in collisional orogens. *J. Petrol.* 56, 227–254.
- Yardley, B.W., 1981. Effect of cooling on the water content and mechanical behavior of metamorphosed rocks. *Geology* 9, 405–408.
- Yardley, B.W.D., Valley, J.W., 1997. The petrologic case for a dry lower crust. *J. Geophys. Res.* 102, 12173–12185.
- Yin, A., Harrison, T.M., 2000. Geologic evolution of the Himalayan-Tibetan orogen. *Annu. Rev. Earth Planet. Sci.* 28, 211–280.
- Yuan, H., Gao, S., Liu, X., Li, H., Günther, D., Wu, F., 2004. Accurate U-Pb age and trace element determinations of zircon by laser ablation-inductively coupled plasma-mass spectrometry. *Geostand. Geoanal. Res.* 28, 353–370.
- Zhang, Z.M., Dong, X., Santosh, M., Zhao, G.C., 2014b. Metamorphism and tectonic evolution of the Lhasa terrane, Central Tibet. *Gondwana Res.* 25, 170–189.
- Zhang, Z.M., Dong, X., Xiang, H., Liou, J.G., Santosh, M., 2013. Building of the Deep Gangdese Arc, South Tibet: Paleocene plutonism and granulite-facies metamorphism. *J. Petrol.* 54, 2547–2580.
- Zhang, L.Y., Ducea, M.N., Ding, L., Pullen, A., Kapp, P., Hoffman, D., 2014a. Southern Tibetan Oligocene-Miocene adakites: a record of Indian slab tearing. *Lithos* 210, 209–223.
- Zhang, S.Q., Mahoney, J., Mo, X.X., Ghazi, A., Milani, L., Crawford, A., Guo, T.Y., Zhao, Z.D., 2005. Evidence for a widespread Tethyan upper mantle with Indian-Ocean-type isotopic characteristics. *J. Petrol.* 46, 829–858.
- Zhang, G.Y., Zheng, Y.Y., Gong, F.Z., Gao, S.B., Qu, W.J., Pang, Y.C., Shi, Y.R., Yin, S.Y., 2008. Geochronologic constraints on magmatic intrusions and mineralization of the Jiru porphyry copper deposit, Tibet, associated with continent-continent collisional process. *Acta Petrol. Sin.* 24, 473–479 (in Chinese with English abstract).
- Zhao, Z.D., Mo, X.X., Dilek, Y., Niu, Y.L., DePaolo, D.J., Robinson, P., Zhu, D.C., Sun, C.G., Dong, G.C., Zhou, S., 2009. Geochemical and Sr-Nd-Pb-O isotopic compositions of the post-collisional ultrapotassic magmatism in SW Tibet: petrogenesis and implications for India intra-continental subduction beneath southern Tibet. *Lithos* 113, 190–212.
- Zhao, J.X., Qin, K.Z., Li, G.M., Li, J.X., Xiao, B., Chen, L., 2012. Geochemistry and petrogenesis of granitoids at Sharang Eocene porphyry Mo deposit in the main-stage of India-Asia continental collision, Northern Gangdese, Tibet. *Resour. Geol.* 62, 84–98.
- Zhao, J.X., Qin, K.Z., Li, G.M., Li, J.X., Xiao, B., Chen, L., Yang, Y.H., Li, C., Liu, Y.S., 2014. Collision-related genesis of the Sharang porphyry molybdenum deposit, Tibet: evidence from zircon U-Pb ages, Re-Os ages and Lu-Hf isotopes. *Ore Geol. Rev.* 56, 312–326.
- Zheng, Y.Y., Duo, J., Wang, R.J., Cheng, S.B., Zhang, G.Y., Fan, Z.H., Gao, S.B., Dai, F.H., 2007a. New advances in the study of the gigantic Gangdise porphyry copper metallogenetic zone, Tibet. *Geol. China* 34, 324–334 (in Chinese with English abstract).
- Zheng, Y.C., Hou, Z.Q., Li, W., Liang, W., Huang, K.X., Li, Q.Y., Sun, Q.Z., Fu, Q., Zhang, S., 2012. Petrogenesis and geological implications of the Oligocene Chongmuda-Mingze adakite-like intrusions and their mafic enclaves, southern Tibet. *J. Geol.* 120, 647–669.
- Zheng, Y.Y., Sun, X., Gao, S.B., Wang, C.M., Zhao, Z.Y., Wu, S., Li, J.D., Wu, X., 2014a. Analysis of stream sediment data for exploring the Zhunuo porphyry Cu deposit, southern Tibet. *J. Geochem. Explor.* 143, 19–30.
- Zheng, Y.Y., Sun, X., Gao, S.B., Wu, S., Xu, J., Jiang, J.S., Chen, X., Zhao, Z.Y., Liu, Y., 2015. Metallogenesis and the mineralogical series in the Gangdese polymetallic copper belt. *J. Asian Earth Sci.* 103, 23–39.
- Zheng, Y.Y., Sun, X., Gao, S.B., Zhao, Z.D., Zhang, G.Y., Wu, S., You, Z.M., Li, J.D., 2014b. Multiple mineralization events at the Jiru porphyry copper deposit, southern Tibet: implications for Eocene and Miocene magma sources and resource potential. *J. Asian Earth Sci.* 79, 842–857.
- Zheng, Y.Y., Xue, Y.X., Cheng, L.J., Fan, Z.H., Gao, S.B., 2004. Finding, characteristics and significances of Qulong superlarge porphyry copper(molybdenum) deposit, Tibet. *Earth Sci.* 29, 103–108 (in Chinese with English abstract).
- Zheng, Y.Y., Zhang, G.Y., Xu, R.K., Gao, S.B., Pang, Y.C., Cao, L., Du, A.D., Shi, Y.R., 2007b. Geochronologic constraints on magmatic intrusions and mineralization of the Zhunuo porphyry copper deposit in Gangdese, Tibet. *Chin. Sci. Bull.* 52, 3139–3147 (in Chinese with English abstract).
- Zhu, D.C., Zhao, Z.D., Niu, Y.L., Dilek, Y., Mo, X.X., 2011b. Lhasa terrane in southern Tibet came from Australia. *Geology* 39, 727–730.
- Zhu, D.C., Zhao, Z.D., Niu, Y.L., Mo, X.X., Chung, S.L., Hou, Z.Q., Wang, L.Q., Wu, F.Y., 2011a. The Lhasa Terrane: record of microcontinent and its histories of drift and growth. *Earth Planet. Sci. Lett.* 301, 241–255.
- Zhu, D.C., Zhao, Z.D., Niu, Y.L., Dilek, Y., Hou, Z.Q., Mo, X.X., 2013. The origin and pre-Cenozoic evolution of the Tibetan Plateau. *Gondwana Res.* 23, 1429–1454.
- Zindler, A., Hart, S., 1986. Chemical geodynamics. *Annu. Rev. Earth Planet. Sci.* 14, 493–571.